

ULTRAVIOLET/X-RAY VARIABILITY AND THE EXTENDED X-RAY EMISSION OF THE RADIO-LOUD BROAD ABSORPTION LINE QUASAR PG 1004+130

A. E. SCOTT^{1,2}, W. N. BRANDT^{1,2,3}, B. P. MILLER⁴, B. LUO^{1,2}, S. C. GALLAGHER^{5,6}

¹Department of Astronomy & Astrophysics, 525 Davey Laboratory, Pennsylvania State University, University Park, PA 16802, USA; amyscott@psu.edu

²Institute for Gravitation and the Cosmos, Pennsylvania State University, University Park, PA 16802, USA

³Department of Physics, 104 Davey Laboratory, Pennsylvania State University, University Park, PA 16802, USA

⁴Department of Chemistry and Physical Sciences, The College of St. Scholastica, Duluth, MN 55811, USA

⁵Department of Physics and Astronomy, University of Western Ontario, London, ON, N6A 3K7, Canada

⁶Visiting Fellow, Yale Center for Astronomy and Astrophysics, Yale University, P.O. Box 208120, New Haven, CT 06520, USA

Accepted 2015 May 5

ABSTRACT

We present the results of recent *Chandra*, *XMM-Newton*, and *Hubble Space Telescope* observations of the radio-loud (RL), broad absorption line (BAL) quasar PG 1004+130. We compare our new observations to archival X-ray and UV data, creating the most comprehensive, high signal-to-noise, multi-epoch, spectral monitoring campaign of a RL BAL quasar to date. We probe for variability of the X-ray absorption, the UV BAL, and the X-ray jet, on month–year timescales. The X-ray absorber has a low column density of $N_{\text{H}} = 8 \times 10^{20} - 4 \times 10^{21} \text{ cm}^{-2}$ when it is assumed to be fully covering the X-ray emitting region, and its properties do not vary significantly between the 4 observations. This suggests the observed absorption is not related to the typical “shielding gas” commonly invoked in BAL quasar models, but is likely due to material further from the central black hole. In contrast, the C IV BAL shows strong variability. The equivalent width (EW) in 2014 is $EW = 11.24 \pm 0.56 \text{ \AA}$, showing a fractional increase of $\Delta EW / \langle EW \rangle = 1.16 \pm 0.11$ from the 2003 observation, 3183 days earlier in the rest-frame. This places PG 1004+130 among the most highly variable BAL quasars. By combining *Chandra* observations we create an exposure $2.5\times$ deeper than studied previously, with which to investigate the nature of the X-ray jet and extended diffuse X-ray emission. An X-ray knot, likely with a synchrotron origin, is detected in the radio jet $\sim 8''$ (30 kpc) from the central X-ray source with a spatial extent of $\sim 4''$ (15 kpc). No similar X-ray counterpart to the counterjet is detected. Asymmetric, non-thermal diffuse X-ray emission, likely due to inverse Compton scattering of Cosmic Microwave Background photons, is also detected.

Keywords: galaxies: active – quasars: individual (PG 1004+130) – quasars: absorption lines – X-rays: galaxies

1. INTRODUCTION

Active Galactic Nuclei (AGN) can significantly affect the properties of their host galaxies through mechanical feedback provided by winds and jets. Fast ($v \sim 0.01 - 0.1c$) outflowing winds manifest themselves observationally as blueshifted, broad absorption lines (BALs) in the UV/optical spectra of $\sim 15\%$ of quasars (e.g., Hewett & Foltz 2003), although it is likely that they exist in most quasars and we only detect them when our line-of-sight passes directly through the outflowing material (e.g., Weymann et al. 1991). As this material is not static, variability is expected in the BALs on a range of timescales characteristic of, e.g., variations in the ionization parameter and/or changes in the flow structure or disk rotation. There have been many studies of the UV variability of BALs in samples of quasars (e.g., Barlow 1993; Lundgren et al. 2007; Gibson et al. 2008, 2010; Capellupo et al. 2011, 2012, 2013; Filiz Ak et al. 2012, 2013; Wildy et al. 2014; Welling et al. 2014). These find that BAL variability is both more common and stronger on longer rest-frame timescales and in weaker and higher velocity BALs, with the dominant parameter being the equivalent width (EW) of the BAL (Filiz Ak et al. 2013).

In the disk-wind scenario, the wind is launched from the accretion disk at $\sim 1000R_g$ and is driven by UV line pressure. For a central source emitting typical levels of X-rays, this requires some “shielding gas” to be located between it and the wind to prevent over-ionization of the

outflow (e.g., Murray et al. 1995; Proga et al. 2000). This gas may be responsible for the absorption commonly observed in the X-ray spectra of BAL quasars which is well fit with either a partially covering and/or a partially ionized absorption model with typical column densities of $N_{\text{H}} \sim 10^{21-23} \text{ cm}^{-2}$ (e.g., Gallagher et al. 2002; Giustini et al. 2008; Fan et al. 2009; Streblyanska et al. 2010). This X-ray absorption is also observed to vary in some cases (Gallagher et al. 2004; Giustini et al. 2011; Saez et al. 2012), possibly as a result of complex dynamics related to rotating, infalling, or outflowing material. Compared with non-BAL quasars of a similar UV luminosity, BAL quasars are underluminous in X-rays (e.g., Green et al. 1995; Green & Mathur 1996; Gallagher et al. 1999, 2006; Brandt et al. 2000), but, after correcting for the effects of absorption, a majority are found to have similar underlying X-ray spectral properties to those of non-BAL quasars (e.g., Gallagher et al. 2002; Page et al. 2005). However, some BAL quasars are likely to be intrinsically X-ray weak (Teng et al. 2014; Luo et al. 2014) and in such cases, shielding gas is not required to ensure launching of the wind.

Approximately 10% of AGN have powerful, highly collimated and relativistic jets which emerge from the inner regions ($\sim 10R_g$) of the AGN and emit strongly at radio and X-ray frequencies via synchrotron and Synchrotron Self Compton (SSC; Band & Grindlay 1986) processes. Radio-loud quasars (RLQs) which possess such jets have higher X-ray luminosities than radio-quiet quasars

(RQQs; e.g., Zamorani et al. 1981; Worrall et al. 1987; Miller et al. 2011; Scott et al. 2011), and flatter (harder) X-ray power-law spectral indices (e.g., Reeves & Turner 2000; Saez et al. 2011) as a result of this additional jet-linked X-ray emission component (Sambruna et al. 1999). X-ray counterparts to extended radio jets have been observed in many AGN (e.g., Sambruna et al. 2004; Worrall 2009; Marshall et al. 2011). Diffuse X-ray emission has also been detected tracing the direction of radio jets and unseen counterjets (e.g., Schwartz et al. 2006) and radio lobes (e.g., Croston et al. 2005) and is likely due to inverse Compton scattering of Cosmic Microwave Background (CMB) photons (IC/CMB) by relativistic jet electrons.

It was originally thought that quasars could not host both a BAL wind and a radio jet (e.g., Stocke et al. 1992). However, many subsequent discoveries of radio-loud (RL) BAL quasars have now been made (e.g., Becker et al. 1997, 2000; Brotherton et al. 1998; Menou et al. 2001) although BALs are still not found in quasars with the highest levels of radio-loudness (e.g., Gregg et al. 2006; Shankar et al. 2008). This suggests that the radio jet and BAL wind may affect each other, despite being emitted from different locations within the AGN. It is perhaps more likely that physical properties of the central engine such as mass accretion rate and the spin of the black hole are responsible for the presence of either phenomenon, although no significant differences in the black hole masses or the Eddington ratios of radio-quiet (RQ) and RL BAL quasars have been found (Bruni et al. 2014). RL and RQ BAL quasars also show similar optical properties (Runnoe et al. 2013; Rochais et al. 2014). However Baskin et al. (2015) suggest that differences in the BAL properties of RQ and RL quasars are due to a softer UV/optical SED, indicated by a lower He II EW, which are preferentially found in RL BALs. BAL variability in RLQs does not depend strongly on radio loudness (Filiz Ak et al. 2013), but lobe-dominated RLQs may show greater fractional BAL variability than core-dominated RLQs (Welling et al. 2014). When considering variability on the same timescales, RLQs show a lower fractional variability than RQQs, $\sim 40 \pm 20\%$ (Welling et al. 2014). RL BAL quasars are X-ray weak compared to RL non-BAL quasars as expected, but to a lesser degree than the difference between RQ BAL and RQ non-BAL quasars. This suggests that the X-ray absorption does not affect all of the jet-linked X-ray emission (Miller et al. 2009).

PG 1004+130 (also known as PKS 1004+13 and 4C 13.41) is one of the best-studied examples of a RL BAL quasar. It is optically bright ($B = 15.8$; Véron-Cetty & Véron 2010), low redshift ($z = 0.2406$, Eracleous & Halpern 2004), and has a black hole mass of $M_{\text{BH}} = 1.87^{+0.36}_{-0.45} \times 10^9 M_{\odot}$ (Vestergaard & Peterson 2006). *International Ultraviolet Explorer* (IUE) and *Hubble Space Telescope* (HST) spectra of PG 1004+130 show blueshifted absorption ($v \sim 10,000 \text{ km s}^{-1}$) in the high-ionization lines O VI, N V, Si IV, and C IV (Wills et al. 1999), and it has a C IV BALnicity index¹ of $\text{BI} \sim 850 \text{ km s}^{-1}$ (Wills et al. 1999). It also shows strong C IV BAL variability, with large fractional changes in EW (Welling et al. 2014).

Like most BAL quasars, PG 1004+130 is X-ray weak

$$^1 \text{BI} = - \int_{25000}^{3000} \left[1 - \frac{f(v)}{0.9} \right] dv$$

where $f(v)$ is the normalized flux as a function of velocity displacement from the rest-frame wavelength of the emission line. The BI does not include the first 2000 km s^{-1} of the absorption trough (Weymann et al. 1991).

and was undetected in an early *Einstein* observation (Elvis & Fabbiano 1984). The first X-ray detection and spectra of PG 1004+130 were obtained with *XMM-Newton* in 2003 and *Chandra* in 2005, and were reported in Miller et al. (2006; hereafter M06). Although the *XMM-Newton* spectrum did not show any significant X-ray absorption, the *Chandra* spectrum obtained 20-months (observed-frame) later, revealed complex X-ray absorption best-fit with a partial-covering model ($N_{\text{H}} = 1.2^{+0.83}_{-0.84} \times 10^{22} \text{ cm}^{-2}$, $f = 0.49^{+0.14}_{-0.26}$, $\Gamma = 1.37^{+0.18}_{-0.22}$). PG 1004+130 has also been observed by the *Nuclear Spectroscopic Telescope Array* (NuSTAR; Harrison et al. 2013). It was weakly detected in the 10–20 keV band, suggesting that the shielding X-ray gas is either Compton thick or that PG 1004+130 is intrinsically X-ray weak, although neither scenario was strongly preferred over the other (Luo et al. 2013). If the absorbing material is Compton thick, we would expect to detect a strong Fe $K\alpha$ emission line, but this is not observed (M06; Luo et al. 2013). Its absence could be due to X-ray emission related to a jet diluting the spectrum (Luo et al. 2013), a scenario also favored by broadband modeling (Kunert-Bajraszewska et al. 2015).

PG 1004+130 is RL with a radio loudness parameter of $R^* = 209$ (Wills et al. 1999; where $R^* = f_{5\text{GHz}}/f_{2500\text{\AA}}$, and $R^* > 10$ indicates a RLQ) and its extended radio emission is of a HYMOR (HYbrid MORphology; Gopal-Krishna & Wiita 2000) nature. The surface-brightness of the radio lobe to the SE decreases outwards i.e., a Fanaroff-Riley I (FRI) classification (Fanaroff & Riley 1974), while the surface-brightness of the NW lobe increases outwards (FR II). This asymmetry is likely due to twin jets propagating into dissimilar large-scale environments, i.e., the density of the surrounding medium is higher to the SE so that the jet is more quickly decollimated (Gopal-Krishna & Wiita 2000). The X-ray imaging analysis reported in M06 revealed an X-ray counterpart to the radio jet extending to the SE $\sim 8''$ from the nucleus and upstream from the peak of the radio jet emission. Large-scale diffuse X-ray emission was also detected, extending 40–50'' outward from the nucleus with a flux of $\sim (4.2-4.5) \times 10^{-15} \text{ erg s}^{-1} \text{ cm}^{-2}$ (assuming a power-law model with $\Gamma = 1.8$; M06).

In this work, we present results from newly obtained X-ray and UV observations of PG 1004+130, and compare them to archival data. This allows us to probe for variability of the X-ray absorption, the C IV broad absorption line, and the X-ray jet emission on month-to-year timescales. By combining multiple *Chandra* observations we obtain the deepest imaging to date of an X-ray jet in a HYMOR radio source, with $2.5\times$ greater sensitivity than the original data used in M06. This allows us to place further constraints on the spatial and spectral properties of the X-ray jet, and larger-scale diffuse X-ray emission. This study of PG 1004+130 represents the most comprehensive, high signal-to-noise (S/N), multi-epoch, X-ray and UV spectral monitoring campaign of a RL BAL quasar, with results applicable to this class of quasars as a whole. A description of our new and archival X-ray and UV observations, and details of the data reduction are given in Section 2. In Section 3 we present an analysis of the X-ray and UV emission from the nuclear source, including the X-ray absorption properties and the C IV BAL variability. In Section 4 we present analysis of the extra-nuclear X-ray jet and diffuse emission. We discuss our results in Section 5 and summarize our conclusions in Section 6. A standard cosmology in which $H_0 = 69.7 \text{ km s}^{-1} \text{ Mpc}^{-1}$, $\Omega_{\Lambda} = 0.7185$, and $\Omega_{\text{M}} = 0.2815$ is assumed throughout (Hinshaw et al. 2013). This gives a luminosity distance to PG 1004+130 of $d_{\text{L}} = 1216 \text{ Mpc}$, and hence

an angular scale of 3.8 kpc per arcsec. Errors quoted on X-ray quantities are 90%, unless otherwise stated.

2. OBSERVATIONS

2.1. *Chandra* Data Reduction

PG 1004+130 has been observed twice with the Advanced CCD Imaging Spectrometer (ACIS; Garmire et al. 2003) on board *Chandra* (Weisskopf et al. 2000). We present results from both a recently obtained 60 ks observation (taken in 2014 Mar) and a 40 ks observation taken in 2005 Jan which was previously reported in M06. Details of both observations are given in Table 1. We reduce each data set in the same, consistent way using CIAO version 4.6.1 (Fruscione et al. 2006) and version 4.6.2 of the CALDB. The `chandra_repro` script is used to apply the latest calibration data. Neither observation suffers from significant background flaring, but we use a standard 3σ clipping of outliers from the 2.4–6 keV light curve to select good-time intervals (GTIs) where the count rate was $\leq 0.23\text{ s}^{-1}$ or $\leq 0.21\text{ s}^{-1}$ in 2005 and 2014, respectively. Improved screening for potential cosmic-ray background events was carried out on the 2014 data which were taken in VFaint mode. Neither observation suffers from pile-up in the nuclear source. We use `specextract` to obtain spectra for the point-like nucleus using a circular extraction region with a $4''$ radius centered on the X-ray source position, and background spectra are extracted from a $16''$ radius circle, offset from the source position. These spectra are binned to a minimum of 20 counts per bin to ensure the validity of χ^2 statistics during the subsequent spectral fitting. Auxiliary response files are generated using the latest calibrations to include the time-dependent quantum-efficiency (QE) degradation due to contamination build-up on the ACIS optical-blocking filter. X-ray spectra of the jet emission are also extracted from a rectangular region of size $6.4'' \times 4.3''$, offset by $8''$ from the nuclear source, and at a position angle² of 130° from the source position in both observations (see Section 4). Background spectra are extracted from the same $16''$ radius circular regions as used previously, but in this case no binning is applied, and the spectra are modeled in XSPEC using the Cash statistic (Cash 1979) due to the low number of counts in the spectra.

2.2. *XMM-Newton* Data Reduction

We also consider two *XMM-Newton* (Jansen et al. 2001) European Photon Imaging Camera (EPIC; Turner et al. 2001; Strüder et al. 2001) observations of PG 1004+130; a more recent 60 ks observation taken in 2013 Nov as part of AO-12 and a 20 ks archival observation from 2003 May, first reported in M06. Neither of these observations were affected by substantial background flaring, therefore GTIs were defined as times where the count rate was $\leq 0.4\text{ s}^{-1}$ in the pn detector and $\leq 0.35\text{ s}^{-1}$ in the MOS detectors (although for the 2013 observation this was reduced to 0.115 s^{-1} to exclude 2 short flares). Final exposure times and details of the observations are given in Table 1. Data from each observation were reduced in a consistent and standard way using SAS version 13.5.0. Spectra of the point-like nucleus were extracted from a circular region with a radius of $24.6''$, as in M06, centered on the source position. Neither observation suffers from pile-up of the nuclear source. Circular regions on the

same CCD but offset from the source with radii of $43''$ and $34''$ were used to extract background spectra from the MOS and pn detectors, respectively. Auxiliary response files and redistribution matrices were generated using `arfgen` and `rmfgen`. The resulting spectra from the two MOS detectors were combined, and both the resulting MOS and pn spectra are binned to a minimum of 20 counts per bin using the `Ftool` `grppha`.³

2.3. *HST* Data Reduction

We used the Cosmic Origins Spectrograph (COS; Green et al. 2012) onboard the *HST* to obtain a current-epoch Near-UV (NUV) spectrum covering $\lambda_{\text{obs}} = 1670 - 2120 \text{ \AA}$ which includes the C IV BAL region of PG 1004+130. A 2562 s exposure was obtained with the G230L grating at a central wavelength of 2950 \AA on 2014 Jan 20. The G230L grating was selected to provide spectral resolution exceeding archival UV observations while spanning the entire C IV emission line and BAL absorption region on the A stripe. The target was centered in the cross-dispersion and along-dispersion directions using an ACQ/PEAKXD and ACQ/PEAKD acquisition sequence. Four focal plane grating offset positions (FPPOS=1–4) were employed to accumulate the spectrum on different regions of the detector. Data were taken in the TIME-TAG mode to retain the arrival time information for each event. Standard pipeline⁴ processing steps were applied, including Doppler correction for the shift induced by the orbital motion of *HST*, non-linearity correction for detector deadtimes at high count rates, flat-field correction for pixel sensitivities, wavelength calibration with a flashed line-lamp, bad pixel flagging, extraction of the background-subtracted one-dimensional spectrum, conversion from counts to flux, and conversion to heliocentric wavelengths. The final spectrum has a S/N ratio of ~ 10 across the C IV BAL. No significant temporal or spectral variability is present over the duration of the observation.

3. X-RAY AND UV ABSORPTION VARIABILITY

3.1. Long-term Light Curve

Figure 1 shows long-term light curves for PG 1004+130. The top panel shows the observed 0.5–8 keV X-ray fluxes (not corrected for Galactic or intrinsic N_{H}), estimated from an absorbed power-law model in which the power-law slope is free to vary. *XMM-Newton* fluxes are shown in red, and *Chandra* fluxes are shown in blue, both with 90% errors. Shown in black is the flux extrapolated from a *NuSTAR* observation in 2012 Oct (Luo et al. 2013), the green arrow indicates a 3σ upper limit from an early *Einstein* observation (Elvis & Fabbiano 1984), and the magenta arrow is an upper limit derived from the *ROSAT* All Sky Survey (Voges et al. 1999). Each was extrapolated to a 0.5–8 keV flux by assuming a power-law slope of $\Gamma = 1.5$, typical of radio-loud AGN (e.g., Reeves & Turner 2000).

The bottom panel shows historical monitoring giving an indication of the typical optical variability (~ 0.5 mag) of PG 1004+130. *V*-band magnitudes are estimated from the unfiltered *P* magnitudes given in Smith et al. (1993), differen-

² All angles are measured from North, through East.

³ <http://heasarc.gsfc.nasa.gov/docs/software/ftools/>

⁴ <http://www.stsci.edu/hst/cos/documents/handbooks/datahandbook/>

Table 1
X-ray Observation Log

Start Time (UTD)	Obsid	Observatory	Detector(s)	Exposure Time (ks)	Nuclear Source Counts ^a	Observed 0.5–8 keV Flux ^b ($\times 10^{-13}$ erg s ⁻¹ cm ⁻²)
2003 May 04 19:06:59	0140550601	<i>XMM-Newton</i>	EPIC-MOS	21.51	1171 ⁺³⁵ ₋₃₄	3.49 ^{+0.17} _{-0.23}
			EPIC-pn	18.08	1574 ⁺⁴¹ ₋₄₀	...
2005 Jan 05 16:44:27	5606	<i>Chandra</i>	ACIS-S	39.29	1763 ⁺⁴³ ₋₄₂	4.87 ^{+0.29} _{-0.30}
2013 Nov 05 05:58:10	0728980201	<i>XMM-Newton</i>	EPIC-MOS	63.14	2399 ⁺⁵⁰ ₋₄₉	2.78 ^{+0.10} _{-0.10}
			EPIC-pn	54.99	3598 ⁺⁶¹ ₋₆₀	...
2014 Mar 20 10:42:47	16034	<i>Chandra</i>	ACIS-S	60.97	1599 ⁺⁴¹ ₋₄₀	3.34 ^{+0.22} _{-0.21}

Notes.

^aThe number of observed counts in the nuclear source extraction region. For *XMM-Newton* this includes counts in the energy range 0.5–10 keV, from a circular extraction region with a radius of 24.6''; for *Chandra* this includes counts in the range 0.5–8 keV from a 4'' radius region.

^bThe observed 0.5–8 keV fluxes are determined from an intrinsically absorbed power-law model. For the *XMM-Newton* observations the MOS and pn spectra are modeled simultaneously giving a single flux estimate.

tial *V*-band photometry given in Garcia et al. (1999), differential *R*-band photometry given in Stalin et al. (2004), photometry from SDSS (York et al. 2000), and unfiltered CCD magnitudes from the Catalina Real-Time Transient Survey (Drake et al. 2009).

There exists a well-known correlation between the X-ray-to-optical power-law slope parameter, α_{OX}^5 (Tananbaum et al. 1979), and the rest-frame UV luminosity, due to the physical interplay between the UV disk photons and the X-ray corona (e.g., Vignali et al. 2003; Strateva et al. 2005; Steffen et al. 2006; Young et al. 2010; Lusso et al. 2010). Adopting $\log l_{2500\text{\AA}} = 30.78$ from Shen et al. (2011), and after correcting for the excess X-ray luminosity expected in RLQ (Miller et al. 2011), an X-ray flux of $F_{0.5-8 \text{ keV}} = (75-95) \times 10^{-13}$ erg s⁻¹ cm⁻² is expected. This is 15–35 \times higher than we observe in any of the 4 *XMM-Newton* and *Chandra* observations showing the persistent X-ray weakness of PG 1004+130.

Flux estimates of the same object measured by the EPIC and ACIS detectors are known to show discrepancies with ACIS measuring fluxes that are typically $\sim 10-15\%$ higher (e.g., Nevalainen et al. 2010; Tsujimoto et al. 2011). The 2005 ACIS flux is $\sim 40\%$ higher than the 2003 flux measured by EPIC, and the 2014 ACIS flux is $\sim 20\%$ higher than the 2013 EPIC flux. These differences, which are larger than those typically expected, are suggestive of a real flux change in the source between the observations, rather than simply calibration differences. When we consider the two *XMM-Newton*, or the two *Chandra* observations separately, which reduces calibration effects, we see a significant⁶ flux decrease on timescales of ~ 8 years in the rest-frame of PG 1004+130. A similarly significant decrease is observed in the hard band flux (2–8 keV). The lower flux measured by *NuSTAR* is also suggestive of a real flux change in the source.

3.2. X-ray Spectral Fitting of the Nuclear Source

The grouped X-ray spectra were fit with physically motivated models using XSPEC version 12.8 (Arnaud 1996). Each spectral model includes absorption fixed at the value of the Galactic component in the direction of the source. This is estimated using equation 7 from Willingale et al. (2013), $N_{\text{H}} = 3.70 \times 10^{20}$ cm⁻² from Dickey & Lockman (1990), and

⁵ $\alpha_{\text{OX}} = 0.38 \log(f_{\text{X}}/f_{\text{O}})$ where f_{X} and f_{O} are the rest-frame flux densities at 2 keV and 2500 Å, respectively.

⁶ 4.5σ for *XMM-Newton* and 6.7σ for *Chandra*.

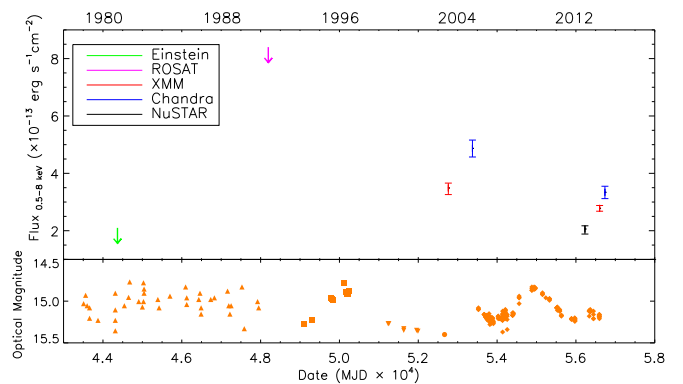


Figure 1. Long-term light curves of PG 1004+130. Top – the observed 0.5–8 keV fluxes estimated from an absorbed power-law model. Fluxes from both *XMM-Newton* observations considered in this work are shown in red, and the fluxes from both *Chandra* observations are shown in blue. Each is plotted with a 90% error bar. The observed 0.5–8 keV flux extrapolated from a *NuSTAR* observation is shown in black (Luo et al. 2013). The green arrow represents a 3σ upper limit from an early *Einstein* observation (Elvis & Fabbiano 1984), and the magenta arrow represents an upper limit from the *ROSAT* All Sky Survey (Voges et al. 1999). Bottom – Filled orange symbols show optical magnitudes from Smith et al. (1993; upwards triangles), Garcia et al. (1999; squares), Stalin et al. (2004; downwards triangles), SDSS (York et al. 2000; circle), and the Catalina Real-Time Transient Survey (Drake et al. 2009; diamonds).

$E(B-V) = 0.0331$ mag from Schlafly & Finkbeiner (2011), resulting in $N_{\text{H}}^{\text{Gal}} = 4.1 \times 10^{20}$ cm⁻². Absorption is modeled using *tbabs* with abundances from Wilms et al. (2000) and cross-sections from Verner & Ferland (1996). Unless stated otherwise, the *XMM-Newton* spectra were modeled over the energy range 0.5–10 keV. The MOS and pn data were fit simultaneously using the same parameters with a freely varying constant added to the model to account for calibration offsets between the two detectors (Mateos et al. 2009). The *Chandra* ACIS spectra were modeled over the energy range 0.5–8 keV.

Each of the 4 data sets was first modeled with a simple power-law fit to the high-energy data (above 2 keV), absorbed only by a Galactic contribution. Figure 2 shows the unfolded spectra (top) and the ratio of the data to this power-law model (bottom). This clearly shows a flat power-law slope, as expected for radio-loud AGN such as PG 1004+130. When the hard-band power-law fit is extrapolated down to 0.5 keV, the presence of intrinsic absorption at lower energies is also clear, and appears to be larger in the *Chandra* spectra than in the

XMM-Newton spectra. Such absorption is expected for BAL quasars (e.g. Gallagher et al. 2002).

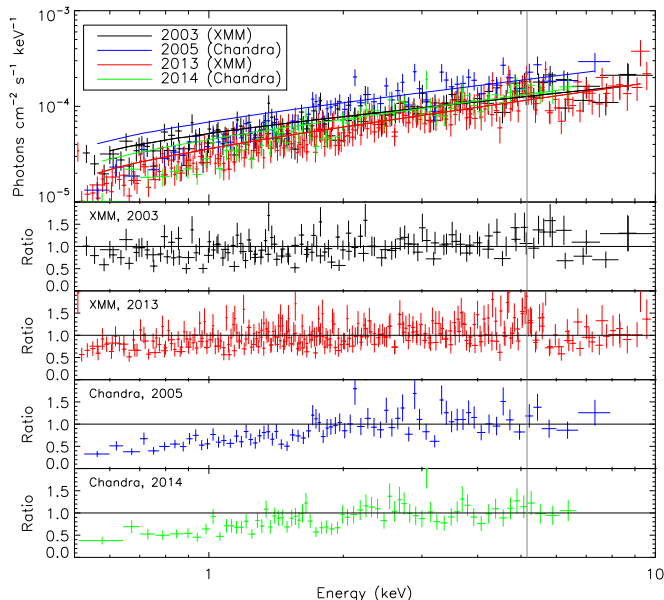


Figure 2. X-ray spectra from each of the 4 epochs. The *XMM-Newton* MOS and pn spectra are fit simultaneously (data from MOS1 and MOS2 are combined) and are plotted in the same color on this figure for clarity. Each of the data sets are modeled with a power law (with only a contribution from Galactic absorption) over 2–8 keV (*Chandra*) and 2–10 keV (*XMM-Newton*). This model is shown extrapolated down to 0.5 keV. The vertical grey line indicates the observed energy at which the neutral iron emission line at a rest-frame energy of 6.4 keV is expected. This feature is visible in the 2013 *XMM-Newton* spectra. The top panel shows the unfolded spectra with $E \times Ef(E)$ plotted on the y-axis such that a power-law slope of $\Gamma = 2$ would be horizontal in the figure. The bottom panels show the ratio of the data to the power-law model, with the residuals at lower energies clearly indicating the absorption present in both *Chandra* spectra, and the 2013 *XMM-Newton* spectra.

We therefore fit each of the data sets with an absorbed power-law, XSPEC model `tbabs*ztbabs*po`, i.e., the absorber at the redshift of the source is both fully neutral and fully covering the source. The best-fitting parameters for each model are listed in Table 2. Confidence contours (at 1, 2, & 3σ) from this absorbed power-law fit are shown in Figure 3, where different colors and linestyles are used for each of the 4 data sets. Crosses mark the location of the fit parameters for which χ^2 is a minimum, although none is shown for the 2003 *XMM-Newton* data as N_{H} is unconstrained in this fit. The results from the two *Chandra* observations (2005, shown in dashed blue, and 2014, shown in solid green) are highly consistent, showing constrained absorption column densities of $N_{\text{H},2005} = (0.19^{+0.10}_{-0.08}) \times 10^{22} \text{ cm}^{-2}$ and $N_{\text{H},2014} = (0.17^{+0.13}_{-0.12}) \times 10^{22} \text{ cm}^{-2}$, respectively. However, there are clear differences between these *Chandra* data and the results from both *XMM-Newton* observations, which show steeper photon indices and lower levels of absorption.

The X-ray detectors of ACIS and EPIC are known to yield different spectral fitting results even during simultaneous observations of the same object, or in observations of non-variable objects (e.g., galaxy clusters; Nevalainen et al. 2010). By comparison with the typical Γ and N_{H} differences found in simultaneous ACIS and EPIC observations of the BL Lac PKS 2155-304 (Ishida et al. 2011), we conclude that the 2013 *XMM-Newton* results are likely to be consistent with both the

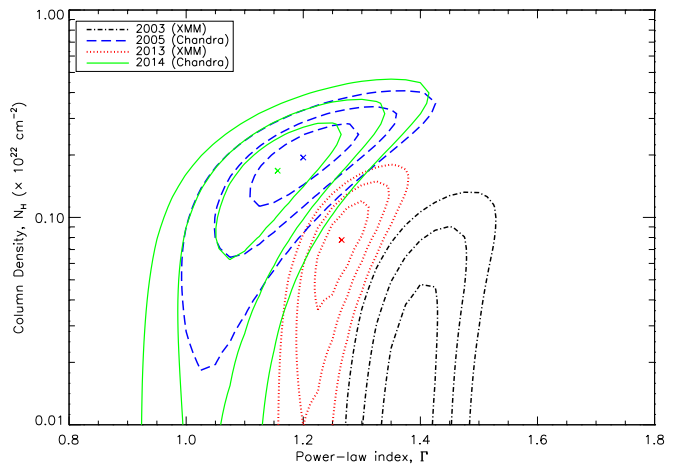


Figure 3. Confidence contours (1, 2 & 3σ), for an absorbed power-law fit (`tbabs*ztbabs*po`) for each of the 4 data-sets. Crosses indicate the fit parameters which give the minimum value of χ^2 . The *Chandra* data appears to be consistent between each epoch. The 2003 *XMM-Newton* data yields significantly different spectral parameters; differences that appear to be larger than those expected from known calibration differences between the detectors. The 2013 *XMM-Newton* data also shows differences, but of a smaller size, such that they may be attributed to calibration effects.

2014 and 2005 *Chandra* observations after accounting for these cross-calibration differences. Only the original 2003 *XMM-Newton* observation appears to show PG 1004+130 with different spectral parameters (Γ , N_{H}). This was previously observed and discussed in M06.

However, the detectability of absorption is dependent on the spectral quality. As the 2003 *XMM-Newton* spectra contain fewer counts than are required to significantly detect absorption of $N_{\text{H}} \sim 0.08 \times 10^{22} \text{ cm}^{-2}$ (the level measured in the 2013 *XMM-Newton* data), 100% of the time (see Scott et al. 2012 for detectability curves), this may be limiting our ability to significantly detect absorption even though it is present in the source. If instead, we fix Γ to the value obtained from the fit to high energies (≥ 2 keV), as shown in Figure 2, we do measure a significant absorption component with $N_{\text{H},2003} = (0.08^{+0.05}_{-0.04}) \times 10^{22} \text{ cm}^{-2}$. This is consistent with the absorption measured in the 2013 *XMM-Newton* data using the same spectral modeling. We therefore suggest that the spectral properties of PG 1004+130 indicated in both *XMM-Newton* observations may be consistent, and therefore the amount of intrinsic absorption has not varied dramatically between all 4 observations.

If each of the data sets are modeled with an absorbed power-law in which Γ is fixed to the values obtained from the fit to high energies (≥ 2 keV), steeper power-law slopes and higher absorption columns are obtained (see Table 2). However, we note that the Γ values remain slightly flatter than expected (e.g., Reeves & Turner 2000), which may indicate that the shape of the underlying continuum above 2 keV is still affected by the absorption. If the spectra are modeled with a power-law using only energies greater than 4 keV, slightly steeper spectral indices are obtained but they remain formally consistent ($\lesssim 1\sigma$) with the previous estimates. Adopting these steeper Γ values in the subsequent absorption modeling leads to a possible increase in the absorption column density of a factor $\lesssim 2$.

Thus far the spectral modeling has only considered absorption due to neutral material that is fully covering the central source. While this is useful for a simple and consistent

Table 2
X-ray Spectral Fitting Results

Data	Model	Γ	N_{H} ($\times 10^{22} \text{ cm}^{-2}$)	f	$\log \xi$ [$\text{erg s}^{-1} \text{ cm}$]	H0 (%)	F-test (%)
<i>XMM-Newton</i> 2003	Power law	$1.37^{+0.05}_{-0.05}$				17.3	
	PL + absorption	$1.36^{+0.07}_{-0.05}$	≤ 0.06			15.7	0
	PL (2–10 keV)	$1.50^{+0.11}_{-0.14}$				82.2	
	PL + absorption	1.50 (fix)	$0.08^{+0.05}_{-0.04}$			7.7	
	PL + partially covering absorber	1.50 (fix)	$4.96^{+11.2}_{-3.46}$	$0.23^{+0.07}_{-0.08}$		18.4	99.7
	PL + ionized absorption	1.50 (fix)	$0.58^{+1.03}_{-0.41}$		$2.09^{+0.48}_{-0.71}$	12.7	97.6
<i>Chandra</i> 2005	Power law	$1.01^{+0.06}_{-0.05}$				8.3	
	PL + absorption	$1.20^{+0.11}_{-0.10}$	$0.19^{+0.10}_{-0.08}$			36.5	99.9
	PL (2–8 keV)	$1.42^{+0.20}_{-0.20}$				19.8	
	PL + absorption	1.42 (fix)	$0.35^{+0.07}_{-0.06}$			12.8	
	PL + partially covering absorber	1.42 (fix)	$1.40^{+0.84}_{-0.59}$	$0.60^{+0.10}_{-0.07}$		36.9	99.8
	PL + ionized absorption	1.42 (fix)	$0.55^{+0.51}_{-0.13}$		$0.89^{+0.58}_{-0.31}$	18.7	94.4
<i>XMM-Newton</i> 2013	Power law	$1.19^{+0.03}_{-0.03}$				27.6	
	PL + absorption	$1.27^{+0.05}_{-0.05}$	$0.08^{+0.05}_{-0.05}$			38.7	99.5
	PL (2–10 keV)	$1.33^{+0.09}_{-0.09}$				44.5	
	PL + absorption	1.33 (fix)	$0.12^{+0.03}_{-0.03}$			34.2	
	PL + partially covering absorber	1.33 (fix)	$0.92^{+1.28}_{-0.66}$	$0.31^{+0.27}_{-0.08}$		40.0	96.3
	PL + ionized absorption	1.33 (fix)	$0.26^{+0.42}_{-0.21}$		$1.42^{+0.66}_{-2.94}$	36.4	87.2
<i>Chandra</i> 2014	Power law	$1.02^{+0.07}_{-0.07}$				45.1	
	PL + absorption	$1.16^{+0.12}_{-0.12}$	$0.17^{+0.13}_{-0.12}$			63.3	98.9
	PL (2–8 keV)	$1.38^{+0.21}_{-0.21}$				93.1	
	PL + absorption	1.38 (fix)	$0.36^{+0.10}_{-0.09}$			36.4	
	PL + partially covering absorber	1.38 (fix)	$1.57^{+1.23}_{-0.77}$	$0.54^{+0.14}_{-0.09}$		62.2	99.7
	PL + ionized absorption	1.38 (fix)	$0.71^{+0.88}_{-0.30}$		$1.27^{+0.55}_{-0.64}$	51.2	97.8

Notes. The spectral fits are carried out using data in the energy range 0.5–10 keV for *XMM-Newton* and 0.5–8 keV for *Chandra*, unless stated otherwise. Parameters are quoted with 90% errors. $\xi = L/nr^2$ with units of $\text{erg s}^{-1} \text{ cm}$; $\log \xi = -3$ for neutral material, and $\log \xi = +6$ for fully ionized material. H0 values greater than 1% indicate the model is an acceptable fit to the data. F -test values greater than 99% indicate that the model including the additional parameter is statistically preferred. Despite differences in the fitting methodology, the best-fitting parameters for the partially covering absorber model for the 2005 *Chandra* data are consistent with those given by M06.

quantification of the amount of absorption present in each observation, the presence of more complex X-ray absorption is thought to be common in both RQ and RL BAL quasars (e.g., Gallagher et al. 2002, 2006; Brotherton et al. 2005). We therefore also fit the spectra with a partially covering absorption model (`tbabs*zpcfabs*po` in XSPEC) and a partially ionized absorption model (`tbabs*zxipcf*po`), in which ZXIPCF (Reeves et al. 2008) is implemented with f fixed at 1.0 to model a partially ionized, but fully covering, absorber. We fix the Γ value to that found for high energies to ensure constrained N_{H} , ξ and f parameters. These are listed in Table 2, along with null-hypothesis probabilities (H0), which if greater than 1% indicate the model is an acceptable fit to the data, and F -test probabilities, for which we say values greater than 99% indicate that the model including the additional component is statistically preferred.

In all 4 observations, the F -test probability and H0 values are higher for the partially covering absorption model than the

partially ionized absorption model, although both provide acceptable fits to the data. For both models the best-fitting spectral parameters are consistent when comparing the 2 *Chandra* observations or the 2 *XMM-Newton* observations. This again suggests that the properties of the X-ray absorption have not changed significantly on long timescales (~ 8 yrs in the source rest-frame).

We test for the presence of iron emission lines in each of our data sets by adding Gaussians to a power-law fit at high energies, i.e., the model `tbabs*(po+zgauss)`. We use the Cash statistic and unbinned spectra as the increased bin size in the grouped data could limit the detection of a narrow line. We fix the width of the line to $\sigma = 0.01$ keV and fix the rest-frame energy of the line to the values 6.4 (for neutral iron), 6.7 (He-like), and 6.9 keV (H-like). In agreement with M06 and Luo et al. (2013), we find no strong evidence for iron emission lines at these energies. We obtain only upper limits on the EW in all cases except for the 6.4 keV

line in the 2013 *XMM-Newton* spectra. This is unsurprising as these spectra have the highest spectral resolution and highest number of counts of all those we consider. The EW measured is $EW_{6.4 \text{ keV}} = 150^{+80}_{-60}$ eV, and the line can be seen in the residuals shown in Figure 2. We also consider a joint fitting of all 6 X-ray spectra (MOS, pn, and ACIS) and obtain $EW_{6.4 \text{ keV}} = 90 \pm 40$ eV (consistent with the upper limit of $EW_{6.4 \text{ keV}} < 105$ eV obtained by M06), $EW_{6.7 \text{ keV}} < 70$ eV, and $EW_{6.9 \text{ keV}} < 70$ eV, suggesting that a low level of neutral iron emission is present.

3.3. Broad Absorption Line Variability

In this section we compare our newly obtained NUV spectrum from *HST* COS to archival spectra taken by *IUE* in 1982 and 1986, and a *HST* Space Telescope Imaging Spectrograph (STIS; Woodgate et al. 1998) spectrum taken in 2003, in order to look for variability of the C IV BAL. Details of all 4 observations are given in Table 3. We also include the S/N of the spectra and the observed UV continuum fluxes, measured between $\lambda_{\text{obs}} = 1750 - 1825$ Å ($\lambda_{\text{rest}} = 1411 - 1471$ Å). With the exception of a $\sim 2\sigma$ flux decrease between the 2003 and 2014 *HST* spectra, there does not appear to be significant variation in the UV flux.

Each of the 4 spectra were modeled with a Voigt profile and a linear function to represent the C IV emission line and the local continuum, respectively. These models are shown by the dashed lines in the top panel of Figure 4. The spectra were then divided by the best-fitting model, resulting in the ratio spectra shown in the bottom panel of Figure 4.

This shows a mini-BAL with a FWHM of 1553 km s^{-1} centered on $\lambda_{\text{rest}} \sim 1542$ Å. The offset of the absorption from the expected emission wavelength of C IV ($\lambda = 1551$ Å) corresponds to a typical outflow velocity of $v_{\text{out}} \sim 1745 \text{ km s}^{-1}$ for the mini-BAL. The BAL has a FWHM of 3372 km s^{-1} (in the 2014 spectrum), indicating a large range of velocities observed along the line-of-sight within the accelerated outflow. These range from $v_{\text{out}} \sim 3700 \text{ km s}^{-1}$ to $v_{\text{out}} \sim 11800 \text{ km s}^{-1}$ ($\sim 0.04c$), with the velocity of the deepest part of the BAL trough being at $v_{\text{out}} \sim 8000 \text{ km s}^{-1}$.

The EW of the BAL and mini-BAL are directly measured from the ratio spectra. The edges of the BAL region are defined as the wavelengths at which the BAL reaches a level which is 90% that of the continuum following the standard definition of Weymann et al. (1991). In the 2014 spectrum this corresponds to a range of $\lambda_{\text{rest}} = 1491 - 1532$ Å for the BAL, and $\lambda_{\text{rest}} = 1537 - 1550$ Å for the mini-BAL. The EW is determined simply as a sum of the flux in all pixels within this region, and the error estimate includes contributions from the continuum placement error, statistical spectral noise, and the uncertainty in the region used. The EW of the BAL and mini-BAL in the newly obtained 2014 spectrum are 11.24 ± 0.56 Å, and 3.38 ± 0.42 Å, respectively. These are listed in Table 3 along with EW estimates for the 3 archival spectra determined by the same method⁷. The final rows of Table 3 compare the EW values of the BAL measured in each of the spectra, with the fractional change in EW being given by

$$\frac{\Delta EW}{\langle EW \rangle} = \frac{EW_{\text{new}} - EW_{\text{old}}}{0.5(EW_{\text{new}} + EW_{\text{old}})}. \quad (1)$$

⁷ We use a different normalization and modeling of the spectra to that of Welling et al. (2014), resulting in slightly different EW values.

Figure 4 (bottom) shows the C IV BALs for each of the 4 spectra, smoothed with a Gaussian of 8 Å width. This clearly shows the strongly variable C IV absorption that PG 1004+130 is known to possess, i.e., the BAL strength increases from the 1982 *IUE* observation (blue) to the 1986 *IUE* observation (red), before diminishing greatly in depth in the 2003 *HST* observation (green). Further, dramatic variability is revealed by the latest 2014 *HST* observation (black), which shows the BAL has deepened. In addition to large changes in EW, the shape of the BAL trough also varies significantly between the observations. In comparison, the mini-BAL at a smaller blueshift shows little variability in both strength or shape, with the exception of the 2003 spectrum in which the trough is much shallower.

The 2014 *HST* spectrum does not cover the wavelength of other possible BAL troughs (e.g., O VI, N V), nor do we see evidence for a Si IV BAL.

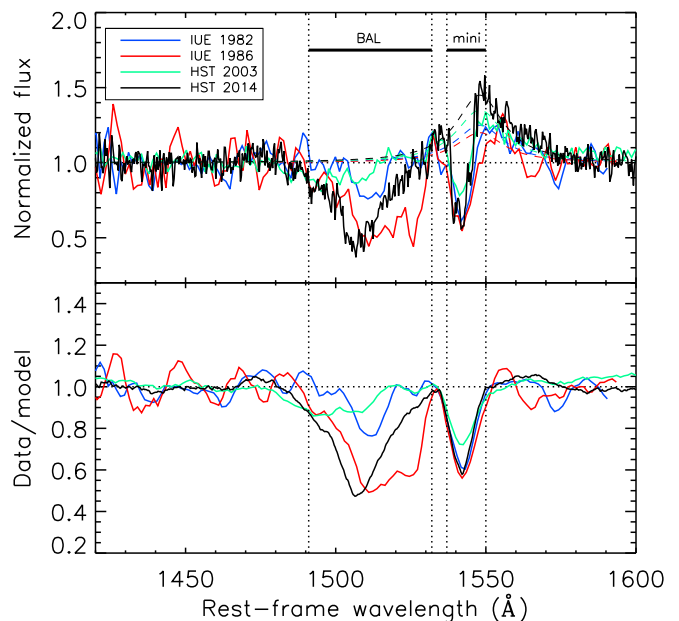


Figure 4. UV spectra of PG 1004+130, covering the C IV emission/absorption-line region. Archival *IUE* spectra from 1982 and 1986 are shown in blue and red respectively, and an archival *HST* STIS spectrum from 2003 is shown in green. Our recent *HST* COS spectrum (2014 Jan) is shown in black. The top panel shows each of the spectra normalized to the same scale. The dashed lines show the best-fitting model for each spectrum, composed of a linear component to model the local continuum, and a Voigt profile for the C IV emission line. The bottom panel shows the resulting ratio spectra after each spectrum has been divided by its best-fitting model. They have been smoothed with a Gaussian of 8 Å width. The regions over which the EW of the BAL and mini-BAL are determined are shown by the vertical, black, dotted lines.

4. EXTRA-NUCLEAR X-RAY EMISSION

The 2005 *Chandra* observation of PG 1004+130 revealed both X-ray emission $\sim 8''$ SW of the nucleus, thought to be related to the FRI radio jet, and diffuse X-ray emission surrounding the source and extending out to $\sim 40 - 50''$ (M06). In this work, we combine the data from both *Chandra* observations giving an increased exposure time of ~ 100 ks ($2.5\times$ deeper than previously) with which to further investigate these features.

Table 3
UV Observations and BAL Parameters

	Observation 1	Observation 2	Observation 3	Observation 4
Date	1982-04-24	1986-01-12	2003-03-31	2014-01-20
MJD	45083	46442	52729	56678
Mission	<i>IUE</i>	<i>IUE</i>	<i>HST</i>	<i>HST</i>
Instrument	STIS	COS
Grating	G230L	G230L
Central wavelength (Å)	2376	2950
Resolution (Å)	~ 6	~ 6	~ 5	~ 1
Exposure time (s)	22260	18900	2292	2562
UV flux ($\times 10^{-15}$ erg s $^{-1}$ cm $^{-2}$)	9.29 ± 0.87	8.03 ± 1.01	8.53 ± 0.41	7.20 ± 0.49
Signal-to-noise (S/N)	10.6	7.7	20.6	14.6
Mini-BAL EW (Å)	3.38 ± 0.32	4.14 ± 0.38	2.74 ± 0.25	3.38 ± 0.42
BAL EW (Å)	3.03 ± 0.56	13.38 ± 0.64	2.98 ± 0.34	11.24 ± 0.56
<i>Comparison of BAL to 2014:</i>				
τ (days)	9346	8251	3183	...
ΔEW (Å)	8.21 ± 0.79	-2.14 ± 0.85	8.26 ± 0.66	...
$\langle EW \rangle$ (Å)	7.14 ± 0.40	12.31 ± 0.43	7.11 ± 0.34	...
$\Delta EW / \langle EW \rangle$	1.15 ± 0.13	-0.17 ± 0.07	1.16 ± 0.11	...
<i>Comparison of BAL to 2003:</i>				
τ (days)	6163	5068
ΔEW (Å)	-0.05 ± 0.66	-10.40 ± 0.72
$\langle EW \rangle$ (Å)	3.01 ± 0.33	8.18 ± 0.36
$\Delta EW / \langle EW \rangle$	-0.02 ± 0.26	-1.27 ± 0.10
<i>Comparison of BAL to 1986:</i>				
τ (days)	1095
ΔEW (Å)	10.35 ± 0.85
$\langle EW \rangle$ (Å)	8.21 ± 0.43
$\Delta EW / \langle EW \rangle$	1.26 ± 0.12

Notes. The UV flux listed is the observed flux between $\lambda_{\text{obs}} = 1750 - 1825$ Å ($\lambda_{\text{rest}} = 1411 - 1471$ Å) located bluewards of the C IV BAL. The bottom rows compare the BAL properties measured in each of the spectra. τ is the time between observations in the rest-frame of PG 1004+130 and is calculated as $\tau = (\text{MJD}_{\text{new}} - \text{MJD}_{\text{old}})/(1 + z)$. $\Delta EW = EW_{\text{new}} - EW_{\text{old}}$ is the change in the EW, and $\langle EW \rangle = 0.5(EW_{\text{new}} + EW_{\text{old}})$ is the average EW. The ratio of these two quantities gives the fractional change listed.

4.1. X-ray Jet Emission

Figure 5 (top left) shows the 0.5–4 keV⁸ X-ray image produced from the addition of the 2005 and 2014 *Chandra* observations. The 2014 data were reprojected onto the co-ordinate system of the 2005 data to account for a 0.7'' offset between the source positions. The spectral extraction regions used for the nuclear source and the X-ray jet emission are indicated by the green circle and rectangle, respectively. The blue contours are produced from 4.9 GHz (6 cm) VLA radio data (Fomalont 1981) with a resolution of 1.5'', and show flux density levels of 0.75 and 1.25 mJy beam $^{-1}$. Figure 5 (bottom left) shows the same X-ray image, but on a larger scale. In this case, radio data from the FIRST survey (Becker et al. 1995) at 1.4 GHz (21 cm) with a resolution of 5.4'' are used to give contours at 1.5, 3, 8, and 15 mJy beam $^{-1}$ (overlaid in blue). This clearly

shows the HYMOR (Gopal-Krishna & Wiita 2000) nature of the radio emission, with the SE jet showing a decreasing surface-brightness (FRI), whereas the NW counterjet shows an increase in surface brightness at larger radii from the nucleus, typical of the FR II class. X-ray emission is observed following the same direction as the SE radio jet, albeit at closer radial distances than the peak of the radio emission.

Figure 5 (top right) shows the central region of the combined 0.5–4 keV X-ray image which has been rebinned to a subpixel size of 0.05'' and adaptively smoothed using a Gaussian kernel to achieve a minimum S/N of 3. X-ray contours corresponding to 0.0005, 0.001, 0.002, 0.005, 0.01, 0.02, and 0.05 counts per square pixel are overlaid in green. These correspond to flux densities between 6.6×10^{-35} and 6.6×10^{-33} erg s $^{-1}$ cm $^{-2}$ Hz $^{-1}$ arcsec $^{-2}$, assuming a photon energy of 1 keV, for which the ACIS QE is ~ 0.5 and the ef-

⁸ There are few counts at energies greater than 4 keV.

fective area is $\sim 400 \text{ cm}^2$.⁹ This image again clearly shows the X-ray knot which lies upstream of the radio jet emission at a distance of $\sim 8''$ (projected distance of 30 kpc) and position angle of 130° from the nuclear source. No similar X-ray emission is observed in relation to the NW counterjet.

Spectra of the X-ray jet emission to the SE of the nuclear source are extracted from each individual *Chandra* observation using the rectangular region shown on Figure 5 (top left). There are 29 X-ray counts (0.5–8 keV) in both the 2005 and 2014 jet spectra, $\sim 2-3$ of which are likely background counts, with some due to the larger-scale diffuse X-ray emission (see Section 4.2). The spectra are modeled with a power law absorbed only by a Galactic contribution. The 2005 spectrum is relatively flat with $\Gamma = 1.63_{-0.57}^{+0.75}$, whereas the 2014 spectrum is comparatively steep, $\Gamma = 2.21_{-0.79}^{+0.99}$. However, due to the large (90%) errors, this variation is not significant (0.9σ). We also simultaneously model both spectra to obtain a better constraint on the power-law slope; $\Gamma = 1.96_{-0.52}^{+0.63}$. A 1.6σ decrease in the flux of the jet is measured, falling from $F_{0.5-8\text{keV},2005} = (5.47_{-1.55}^{+2.09}) \times 10^{-15} \text{ erg s}^{-1} \text{ cm}^{-2}$ to $F_{0.5-8\text{keV},2014} = (2.86_{-1.12}^{+2.04}) \times 10^{-15} \text{ erg s}^{-1} \text{ cm}^{-2}$. This variation is largely due to the difference in the best-fitting model as when Γ is fixed to 1.96 for each observation, the measured fluxes differ by only $\sim 1\sigma$ and show a decrease of $\sim 30\%$.

Radial surface-brightness profiles for the SE X-ray jet emission were created from the 0.5–4 keV X-ray images which were first rebinned to a sub-pixel size of $0.05''$. Concentric annular sectors covering a 30° arc from $115-145^\circ$, with a thickness of $1''$ were used to determine the jet profile. Figure 6 (top left) compares the jet profiles from the 2005 (black) and 2014 (red) observations. This shows that the distribution of the X-ray emission has not varied significantly between the 2 epochs. An increase in the X-ray surface brightness is clear at $\sim 8''$ from the nuclear source, corresponding to the peak of the X-ray jet emission. This knot is also clearly extended by $\sim 4''$. Figure 6 (top right) shows the jet profile from the combined 2005 and 2014 data (black). This is compared to a profile created from the remaining 330° of the annular sectors (red). This clearly shows the excess X-ray surface brightness to the SE, which is significantly higher than the background level (estimated from a $8'' \times 8''$ box and indicated by the dashed blue line).

4.2. Diffuse X-ray Emission

Figure 5 (bottom right) shows the wider-scale X-ray image, smoothed in the manner described in the previous section. This image shows more clearly the low-level diffuse X-ray emission surrounding PG 1004+130 which was previously reported by M06. The emission largely appears to follow the direction of the SE FRI jet and the NW FRII counterjet, rather than forming a spherical halo around the nuclear source. The diffuse X-ray emission to the SE appears to trace the full extent of the lobe, and extends out to $\sim 65''$, corresponding to a projected distance of ~ 250 kpc. The emission to the NW extends out a similar distance as to the SE ($\sim 55'' \approx 210$ kpc), but does not trace the full extent of the FRII radio lobe. The X-ray emission to the NW is also weaker than to the SE. There are 129_{-22}^{+24} , 0.5–4 keV background-subtracted counts in a 50° wedge to the SE, extending from

$16''$ to $63''$ (marked on Figure 5, bottom right, in green)¹⁰, and 86_{-21}^{+24} counts in a similar wedge along the NW counterjet. The contributions from point sources have been excluded and the values are corrected for any subsequent loss of area. Owing to the increased exposure time of the combined observations, and the subsequent increase in counts, we are able to conduct a basic spectral analysis of the diffuse emission. We extract spectra from the SE and NW wedge regions and bin them to a minimum of 15 counts per bin using *grppha*. A power-law model gives $\Gamma = 1.65_{-0.74}^{+0.89}$, $\chi^2/\nu = 19.6/13$ and a flux of $F_{0.5-4\text{keV}} = (1.02_{-0.25}^{+0.26}) \times 10^{-14} \text{ erg s}^{-1} \text{ cm}^{-2}$ ($L_{0.5-4\text{keV}} = 1.81_{-0.44}^{+0.46} \times 10^{42} \text{ erg s}^{-1}$) for the SE emission and $\Gamma = 1.95_{-1.05}^{+1.67}$, $\chi^2/\nu = 9.9/10$ and $F_{0.5-4\text{keV}} = (4.82_{-1.80}^{+2.55}) \times 10^{-15} \text{ erg s}^{-1} \text{ cm}^{-2}$ ($L_{0.5-4\text{keV}} = 8.56_{-3.2}^{+4.5} \times 10^{41} \text{ erg s}^{-1}$) for the NW emission. This confirms the lower flux of the NW emission, and gives consistent power-law slopes. Although we cannot formally reject a bremsstrahlung model (it gives similar reduced χ^2 values and $H0 > 1\%$), the kT value obtained is unconstrained, tending to higher temperatures and thus a power-law distribution.

Figure 6 (bottom) shows the radial surface-brightness profiles of the diffuse X-ray emission. The numbers of counts were extracted from 15 concentric arcs with equal thickness between a radius of $0-60''$. The profile of the SE diffuse emission (shown in black) was extracted from a 50° arc between angles 95° and 145° , the diffuse emission along the NW counterjet (shown in red) was extracted from a 50° arc between angles 275° and 325° , and remaining portions of the arcs are used for the comparison profile (shown in green). The background level (shown by the blue, dashed line) was estimated from a $30'' \times 30''$ box at a distance $> 80''$ from the central source position. This figure shows that the X-ray surface brightness along the jet and counterjet directions is higher than that in the remaining directions. The surface brightness of the SE diffuse emission is also generally higher than that of the NW emission, although not significantly at each radius. In general, both profiles show a smooth decrease with increasing radial distance from the source.

5. DISCUSSION

5.1. The Nature of the X-ray and UV Absorption

The X-ray absorption commonly observed in BAL quasars may be due to “shielding gas” located close to the central black hole which prevents the over-ionization of the BAL wind (e.g., Murray et al. 1995; Proga et al. 2000; Gibson et al. 2009; Wu et al. 2010). Quasar-wind simulations suggest this gas should be variable on timescales of months-to-years (e.g., Sim et al. 2010, 2012). X-ray absorption variability has been observed in some BAL quasars such as PG 2112+059 which showed a dramatic increase in column density over 3 yrs (Gallagher et al. 2004), and PG 1126–041, a mini-BAL quasar which showed rapid variability on timescales of months-to-hours due to highly ionized absorbers (Giustini et al. 2011). However, in the sample of 11 BAL quasars studied systematically by Saez et al. (2012), exceptional X-ray variability (e.g., uncovering events where the shielding gas largely moves out of the line-of-sight), compared to non-BAL quasars, was not seen.

In this work we have shown that the X-ray absorption properties of PG 1004+130 measured in 4 observations taken up

⁹ <http://cxc.harvard.edu/proposer/POG/html/chap6.html> (*Chandra* handbook, chapter 6)

¹⁰ Note that the SE region used here differs slightly from that used by M06, as the X-ray emission appears to be diametrically opposed to the NW emission in this deeper exposure.

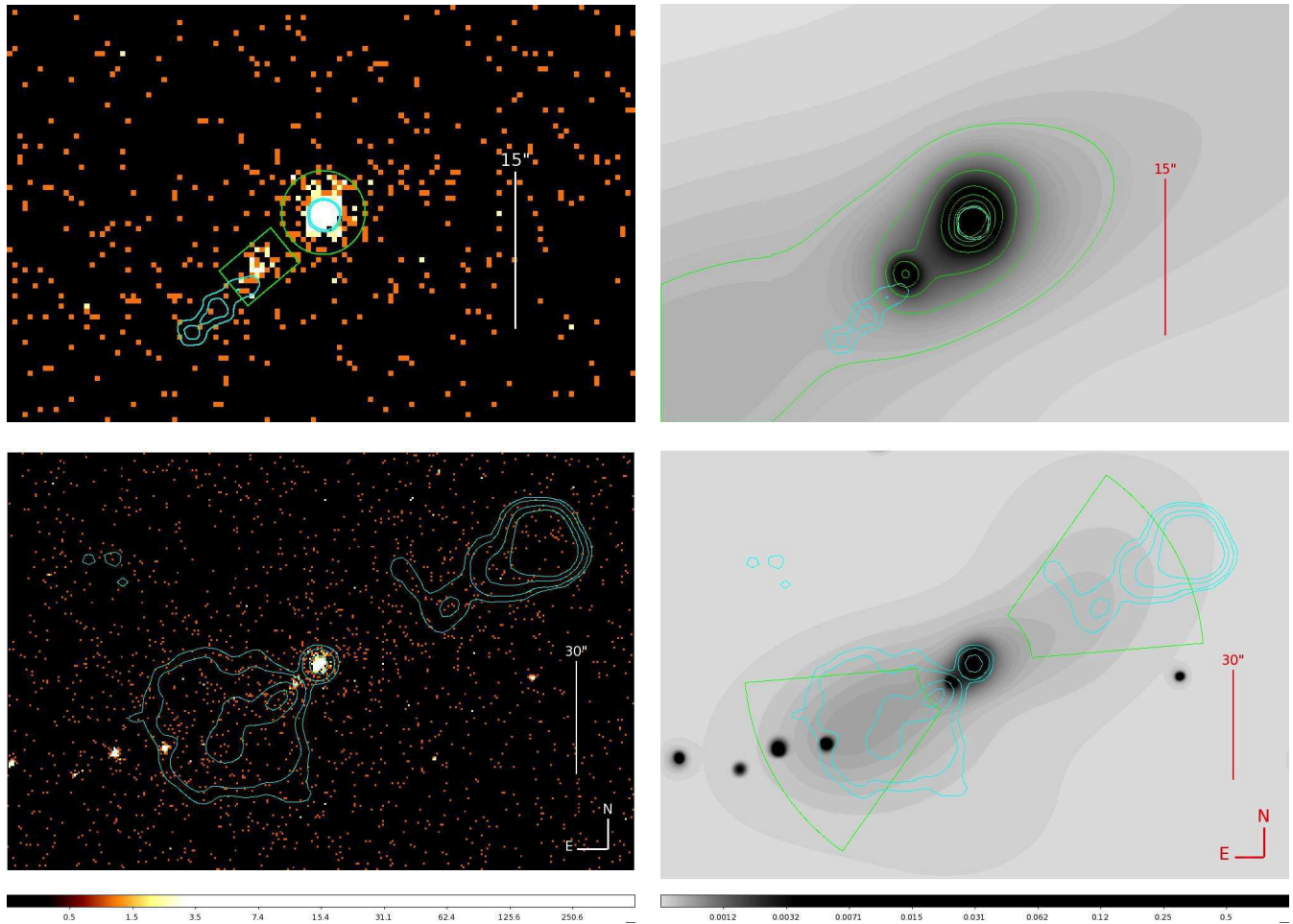


Figure 5. Top left – 0.5–4 keV X-ray image from the combined 2005 and 2014 *Chandra* observations. The X-ray emitting nuclear source and the X-ray knot in the SE jet are clearly visible, and the extraction regions used for the nuclear source (circle) and the jet (rectangle) are shown in green. Radio contours from the VLA at 4.9 GHz (6 cm) corresponding to 0.75 and 1.25 mJy beam⁻¹ are overlaid in blue. Top right – An adaptively smoothed version of the top left image. Shown in green are X-ray contours corresponding to count rates of 0.0005, 0.001, 0.002, 0.005, 0.01, 0.02, and 0.05 counts per square pixel. Blue contours show the same VLA data as in the top left image. Bottom left – The same 0.5–4 keV X-ray image shown in the top left image, but including the extended regions of the system. Blue contours show lower angular resolution radio data from FIRST (at 1.4 GHz/21 cm) at 1.5, 3, 8, and 15 mJy beam⁻¹. Bottom right – An adaptively smoothed version of the bottom left image. The black dots to the SE and W are unrelated X-ray sources, likely background AGN. The green wedges correspond to those used to determine the amount of diffuse X-ray emission along the paths of the SE jet and NW counterjet. The blue contours show the same FIRST data as in the bottom left image. At the redshift of PG 1004+130, 15'' corresponds to a projected physical distance of 57 kpc.

to 8.8 yrs (rest-frame) apart do not differ substantially, regardless of the spectral model used. When a fully covering and neutral absorber is assumed, the column densities range from $N_{\text{H}} = 8 \times 10^{20} - 4 \times 10^{21} \text{ cm}^{-2}$, which are among the lowest values typically observed (Gallagher et al. 2002; Giustini et al. 2008; Fan et al. 2009; Streblyanska et al. 2010). However, the power-law slopes obtained in the modeling are $\Gamma \leq 1.5$, perhaps indicating that the true levels of absorption in the source may be higher by a factor of ~ 2 (see Section 3.2). In the case of a partially covering absorber, the column densities obtained are naturally higher, $N_{\text{H}} \sim 10^{22} \text{ cm}^{-2}$, and more consistent with those for other BAL quasars. The X-ray absorption can be well modeled with either a partially covering, or an ionized, absorber (see Table 2) and the spectral parameters of these models (N_{H} , f , and ξ) are also consistent for each observation.

As the X-ray absorption properties do not appear to vary, the absorption is perhaps more likely to be due to material located further from the central source, rather than the typi-

cal shielding gas expected on small scales. In the case that PG 1004+130 is intrinsically X-ray weak, such a shield is not required to ensure launching of the BAL wind. Alternatively, if PG 1004+130 is intrinsically X-ray normal, the shielding gas is required to be highly Compton-thick ($N_{\text{H}} \approx 7 \times 10^{24} \text{ cm}^{-2}$; Luo et al. 2013). Absorption with column densities this high would not be detectable in *Chandra* or *XMM-Newton* spectra as all X-rays below ~ 10 keV would be absorbed. In both scenarios the X-ray emission we observe is therefore predominantly from the jet; either because the continuum source is weak in comparison, or because we only see X-rays from the portion of the jet extending beyond the shielding gas. This X-ray emission may then be absorbed by material further from the black hole, naturally explaining the lack of variability and lower column densities observed. However, we cannot rule out variability occurring at a level below that which we are able to significantly detect with our spectra. A column density increase of more than a factor of 2 would be detected as a 3σ change between the *Chandra* spectra.

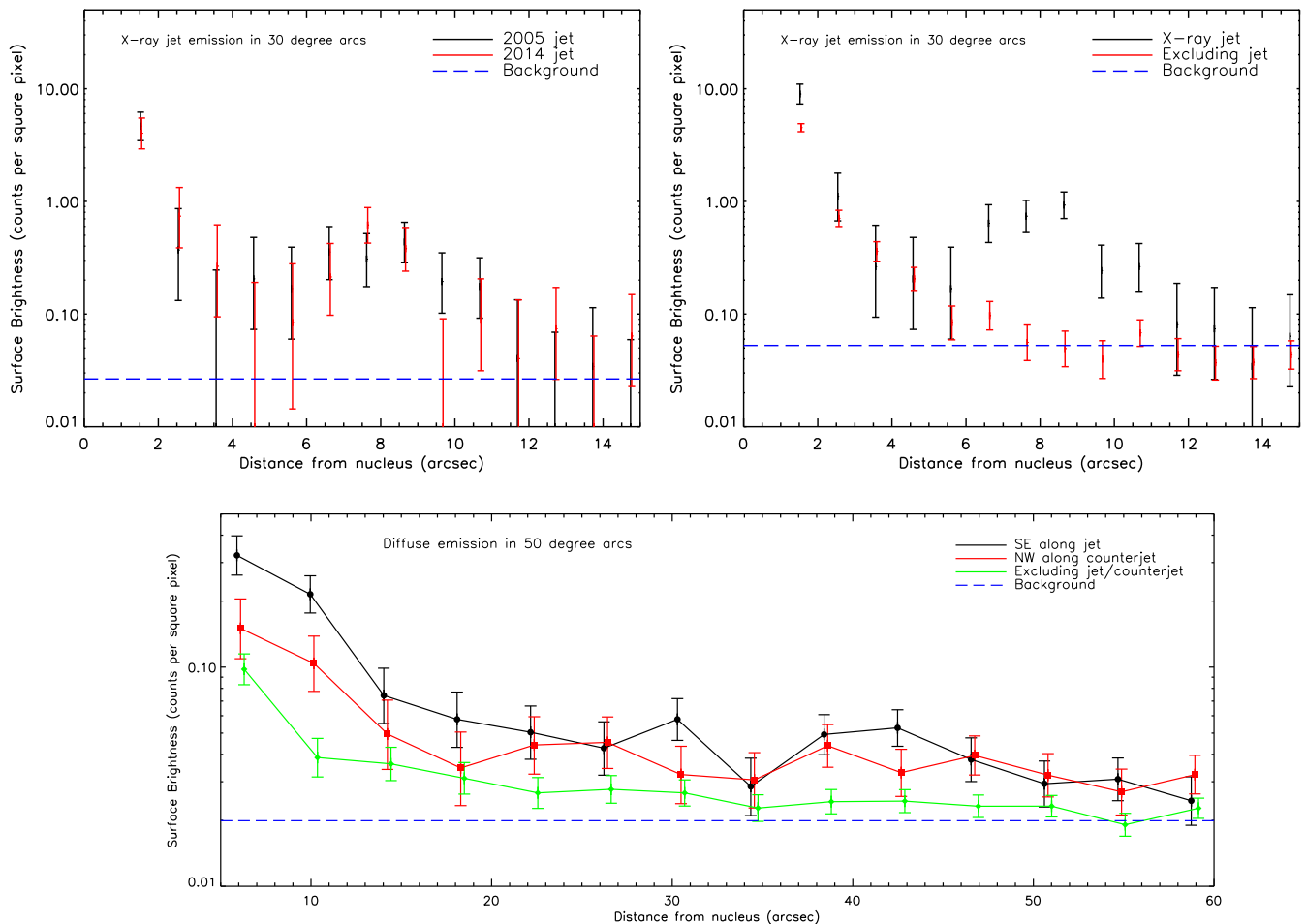


Figure 6. Radial surface brightness profiles. In each case the profiles are extracted from the 0.5–4 keV *Chandra* images which were rebinned to a sub-pixel bin size of $0.05''$. Surface brightnesses are calculated as the number of counts per square pixel and the Gehrels (1986) formulation of errors is used. Top left – A comparison of the SE jet profiles for the 2005 data (black) and the 2014 data (red), extracted from concentric 30° arcs at angles of $115\text{--}145^\circ$, centered on the source position, and with a thickness of $1''$. The blue dashed line gives an indication of the background level (~ 0.02 counts per square pixel in 2005, ~ 0.03 counts per square pixel in 2014) which is determined from an $8'' \times 8''$ box. Top right – The SE jet profile extracted from the combined 2005 and 2014 *Chandra* observations (black), using the same regions as in the top left panel. The profile shown in red is extracted from the remaining 330° annular sectors for comparison. The blue dashed line indicates the background level (~ 0.05 counts per square pixel in the combined data). Bottom – Profiles of the diffuse X-ray emission extracted from concentric 50° arcs to the SE (black) and NW (red). These are compared to a profile extracted from the remaining 260° from each concentric ring (green). Fifteen equal-thickness rings are used from $0\text{--}60''$ radial distance from the central source position. The blue, dashed line indicates the background level (0.02 counts per square pixel) determined from a $30'' \times 30''$ box.

In the scenario in which PG 1004+130 is intrinsically X-ray normal and is absorbed by Compton-thick shielding gas, a strong Fe $K\alpha$ emission line at 6.4 keV with an EW of 1000–2000 eV is expected (e.g., Ghisellini et al. 1994; Matt et al. 1996). Although we do measure a low level of neutral iron emission in a joint fitting of all 4 X-ray spectra ($EW_{6.4\text{ keV}} = 90 \pm 40$ eV; see Section 3.2), it is not as strong as might be expected. This may be due to the dilution of the spectrum by jet-linked X-ray emission (Luo et al. 2013).

The X-ray light curve in Section 3.1 shows significant flux variability between the 4 X-ray observations. Given the constant level of X-ray absorption present, these changes are more likely related to intrinsic variations within the continuum source itself (in the case that PG 1004+130 is intrinsically X-ray weak), or fluctuations in the jet.

In stark contrast to the X-ray absorption properties, the C IV BAL in PG 1004+130 shows large-amplitude variability. The archival observations we compare with our newly obtained *HST* COS spectrum probe rest-frame timescales of $\approx 3\text{--}26$ yrs during which large absolute and fractional

changes in EW are observed (see Table 3). However, the largest changes are between the 2003 and 1986 spectra, i.e., $\Delta EW = -10.4 \pm 0.72 \text{ \AA}$ and $\Delta EW / \langle EW \rangle = -1.27 \pm 0.10$. The magnitudes of these changes place PG 1004+130 among the most variable RL and RQ BAL quasars (e.g., Filiz Ak et al. 2013). Our measurements probe long rest-frame timescales, on which BAL variability is observed to be stronger (see Section 1). In Figure 7 we compare the absolute and fractional BAL variability of PG 1004+130 (red, solid points) to the sample of RL BAL quasars presented in Welling et al. (2014; open black circles). This highlights the large variability of PG 1004+130 in relation to other RL BAL quasars, even despite the longer rest-frame timescales probed by our observations.

Variability in BAL troughs is likely caused by 2 main effects; clumps of material in the outflow moving across our line-of-sight to the continuum source, or the material responding to changes in the incident ionizing radiation. When only portions of the BAL trough spanning a narrow velocity range show changes, perhaps with some portions strengthening

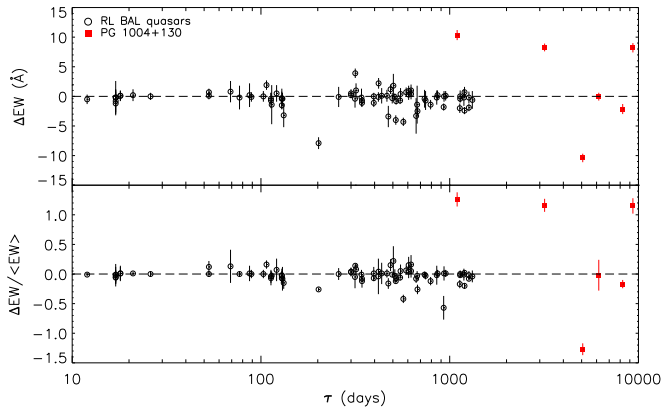


Figure 7. The C IV BAL variability in PG 1004+130, and other RL BAL quasars. Filled red squares show the values for PG 1004+130 and open black circles show values from the sample of RL BAL quasars presented in Welling et al. (2014) — excluding PG 1004+130. The top panel shows the relationship between the absolute variability and rest-frame time interval. The bottom panel shows the fractional variability.

while others weaken (e.g., Gibson et al. 2008; Capellupo et al. 2012), clouds at different velocities, and hence distances from the continuum source, entering and leaving the line-of-sight is a plausible explanation, although it could also be a result of velocity-dependent optical depths (Capellupo et al. 2012). However, many observations of BALs show co-ordinated changes in separate troughs of the same ion, for example, distinct C IV BAL troughs tend to strengthen or weaken together (Filiz Ak et al. 2013). In this case, variations occurring over such a large velocity range are unlikely to be the result of co-ordinated movements within the outflow which would disperse the structure (e.g., Rogerson et al. 2011). Instead, these, and global changes in which the entire profile of a single wide BAL trough varies uniformly (e.g., Grier et al. 2015), are likely a result of a change in the ionizing EUV continuum. However this can only occur if the absorption trough is not too highly saturated. Portions of the trough with low optical depths may show larger variations as they are more susceptible to changes in ionization, than those with only moderate optical depths.

The changes observed in the BAL profile of PG 1004+130 suggest a combination of these scenarios. This is most apparent when considering the BAL trough in the 1986 observation, which appears to be comprised of a main trough centered on $\lambda_{\text{rest}} \sim 1511 \text{ \AA}$ ($v_{\text{out}} \sim 7830 \text{ km s}^{-1}$) and an additional absorption feature with a smaller blueshift superimposed. This component, at $\lambda_{\text{rest}} \sim 1526 \text{ \AA}$ ($v_{\text{out}} \sim 4870 \text{ km s}^{-1}$), does not appear in the other 3 observations (there is a hint of a similar component in the 1982 spectrum but its depth is within 10% of the continuum level and could therefore be noise), and its narrow width suggests it may be due to cloud of material in the line-of-sight during the observation. Making the assumptions that such a cloud is spherical, moving perpendicular to the line-of-sight and passing in front of a negligible size source, we can place an upper limit on the radius of the cloud of $r \lesssim 1.3 \times 10^{17} \text{ cm} \lesssim 0.04 \text{ pc}$, as it must have traveled at least its diameter, at $v \sim 4870 \text{ km s}^{-1}$, in the 6163 day period.

The remainder of the BAL trough in the 1986 spectrum has a similar shape to that in 1982, although both the width and depth have increased by more than a factor of 2. Such a monolithic change is more likely to be the result of the entire outflow varying in response to a change in the ionizing continuum. However, the UV flux does not change

significantly between these observations. Similarly, there is no significant flux difference between the 1986 and 2003 observations, despite a large decrease in the BAL strength, $\Delta EW = -10.40 \pm 0.72 \text{ \AA}$. The flux decrease between the 2003 and 2014 observations is only significant at 2σ but does correspond to a strengthening of the BAL ($\Delta EW = 8.26 \pm 0.66 \text{ \AA}$). The correlation between the observed UV flux and BAL EW may not be as strong as expected as the flux is measured over $\lambda_{\text{rest}} = 1411 - 1471 \text{ \AA}$. While this should give an indication of the UV flux variability, it is not directly measuring the unobservable EUV range which would be responsible for any changes within the outflow. Previous observations have shown the EUV flux can vary more than the UV flux at longer wavelengths (e.g., Marshall et al. 1997).

If a change in the ionizing continuum is the main contributor to the BAL variability, we might expect to see co-ordinated variations in the mini-BAL. This feature is centered on $\lambda_{\text{rest}} \sim 1542 \text{ \AA}$ corresponding to an outflow velocity of $v_{\text{out}} \sim 1745 \text{ km s}^{-1}$ which is over 10000 km s^{-1} slower than parts of the BAL trough. Figure 4 shows that the mini-BAL in the 2003 *HST* spectrum is significantly weaker than in the other 3 spectra. This corresponds well to the BAL which is also extremely weak in this spectrum. However, in general, this feature shows much less variability than the BAL; in particular there is no corresponding deepening in 1986 or 2014 when the BAL is considerably stronger. This is likely due to the feature being more highly saturated, and therefore less susceptible to changes in the ionizing continuum, but may also suggest that material is indeed physically distinct from the higher velocity BAL and likely located much at a much greater distance from the central source.

The 2014 BAL trough shows a similar shape to the main BAL trough in the 1986 spectrum, but is offset in wavelength. This could be due to an acceleration of the entire outflow of $a \approx 0.11 \text{ cm s}^{-2}$, which is consistent with accelerations observed in other BAL quasars (e.g., Vilkovskij & Irwin 2001; Rupke et al. 2002; Gibson et al. 2008).

In the standard model for BAL quasars the wind properties should depend on the X-ray/UV SED and the properties of the shielding gas. Indeed, C IV BALs are observed to be stronger and to have higher velocities in quasars with greater levels of X-ray absorption indicating that the shielding gas plays an important role in determining the properties of the outflowing wind (Brandt et al. 2000; Laor & Brandt 2002; Gallagher et al. 2006; Gibson et al. 2009; Wu et al. 2010). In PG 1004+130 the amount of X-ray absorption does not vary significantly with time, but despite this, large differences in the BAL EW are created. This further suggests that the X-ray absorption we observe is not due to the typical shielding gas. The X-ray absorption could be due to the BAL outflow itself. The presence of the C IV ion in the UV material requires an ionization parameter in the range $\log \xi \sim -0.3$ to $+1.4$ (e.g., Kallman & McCray 1982). This is consistent with the values observed when the X-ray absorption is modeled with a partially ionized model (see Table 2).

We are unable to test for any relation between the X-ray flux and the EW of the UV BAL as only 2 UV and X-ray observations were made at similar epochs. However, despite large differences in EW, the X-ray flux is similar in each case, suggesting no relationship. This is perhaps not unexpected as the observed X-ray emission in PG 1004+130 is likely mostly from a small-scale jet (either because the continuum source is X-ray weak, or the X-ray normal continuum source is absorbed by Compton-thick shielding gas). This flux may

not be expected to influence the BAL production strongly.

5.2. Nature of the Extra-nuclear X-ray Emission

X-ray emission from extended jets has now been detected in over 100 AGN,¹¹ but the physical processes involved in its production are still often uncertain. PG 1004+130 shows such X-ray emission, a knot, in the same direction as the SE FRI radio jet; i.e., at a PA of 130° located at a distance of 8'' (30 kpc) from the core. No X-rays are detected in relation to the NW FRII radio counterjet, but this is not unusual; the majority of detected X-ray jets are one-sided, with the X-rays corresponding to the brighter of the radio jets (Worrall 2009). The HYMOR radio nature is often interpreted as a difference in the environment on either side of the quasar; i.e., the jet propagating into a denser medium to the SE is quickly decollimated giving the FRI appearance, whereas the jet propagating to the NW through a more tenuous medium appears as an FRII (e.g., Gopal-Krishna & Wiita 2000). Shocks, created when the jet collides with an obstacle (e.g., Blandford & Koenigl 1979), accelerate electrons which then cool by emitting synchrotron X-rays and appear as bright X-ray knots. This scenario naturally explains why knots are commonly observed in FRI jets (Worrall 2009) as the probability of such shocks occurring is greater due to the higher density of the medium.

Some X-ray knots have shown exceptional variability, such as the knot in the jet of M87 which increased in intensity by 50% over 5 yrs (Harris et al. 2006). However, no evidence for variability was observed in the X-ray knots in Cen A (Goodger et al. 2010), or in the quasar 3C 273 (Jester et al. 2006). Although the knot in PG 1004+130 does not show substantial variability between the 2 *Chandra* observations, the 1.6 σ decrease in flux (a factor of 2 in ~ 7.5 rest-frame years) is consistent with electrons that have been excited in a shock and are cooling via synchrotron emission, with typical loss-times for such electrons being \sim tens of yrs. Expected power-law spectral indices for this synchrotron emission are $\Gamma \sim 1.6$ (Achterberg et al. 2001), which steepen to $\Gamma \sim 2.1$ when energy losses become more important. Although we do not see a significant difference in the power-law slope between observations, largely owing to the low number of counts in the spectra and hence large errors on the parameter, the values we observe are broadly consistent with this scenario.

However, the X-ray knot is spatially extended by 4'' (15 kpc). Since the loss-times of the electrons are too short for them to diffuse across this distance before emitting X-rays, the emission is likely being produced from a combination of multiple shock sites. This may explain why the flux decrease (and Γ increase) is not highly significant, as we are observing the combined properties of these sites.

We note that in alternative models for the X-ray emission such as beamed IC/CMB (Tavecchio et al. 2000; Celotti et al. 2001), no flux drop is expected as the typical loss-times for the lower-energy electrons involved are $\sim 10^6$ yrs. This scenario is also disfavored as the jet in PG 1004+130 is likely inclined at $\theta \gtrsim 45^\circ$ (M06) implying little line-of-sight beaming.

The peak of the X-ray knot emission lies closer to the core than the peak of the radio jet emission. Offsets such as this are also commonly observed in other sources (e.g., Harris & Krawczynski 2006), and are often explained as a single population of electrons cooling by emitting radiation at progressively lower frequencies from X-ray to ra-

dio as they propagate downstream along the jet (Bai & Lee 2003; Hardcastle et al. 2003). In such a scenario optical emission may be expected between the X-ray and radio peaks, but this is not observed in *HST* imaging of PG 1004+130 (Bahcall et al. 1997; Miller et al. 2006). This perhaps indicates that the X-ray and radio emission instead originate from different electron populations.

The deeper combined exposure time of both *Chandra* observations allows us to further constrain the nature of the diffuse X-ray emission which was previously observed in M06. Figure 5 (bottom right) shows some of this emission extending to a radial distance of 65'' (250 kpc) from the core to the SE, underlying the same area in which the broad FRI radio emission is observed, which includes both the jet and the lobe. Similar emission is observed to the NW, although it only extends to 55'' (210 kpc) and hence does not trace the location of the FRII lobe which is located further from the quasar. This suggests that the diffuse X-ray emission in PG 1004+130 is more closely related to the radio jet emission, rather than the lobes. The possible detection of a radio counterjet on small scales (C. C. Cheung, 2014, private communication) also agrees with this interpretation.

X-ray spectra of the diffuse emission, extracted from the green wedges shown on Figure 5 (bottom right), are well-fit with a power law. This suggests that non-thermal processes are responsible for the diffuse emission, a likely origin being unbeamed IC/CMB. The diffuse X-ray emission is stronger to the SE ($L_{0.5-4\text{keV}} = 1.81^{+0.46}_{-0.44} \times 10^{42} \text{ erg s}^{-1}$) than the NW ($L_{0.5-4\text{keV}} = 8.56^{+4.5}_{-3.2} \times 10^{41} \text{ erg s}^{-1}$). This is consistent with the distribution of colder gas implied by the HYMOR nature of PG 1004+130, which is likely responsible for the stronger radio jet to the SE and the weaker counterjet to the NW. Electrons produced in the IC/CMB model are of a relatively low energy, and hence have lifetimes of $\sim 10^6$ yrs allowing them to travel large distances before emitting X-rays. The diffuse emission could therefore have an origin related to the jet and counterjet, but be located surrounding the radio jet as observed.

6. SUMMARY

We have presented new *Chandra*, *XMM-Newton*, and *HST* COS observations of the RL BAL quasar PG 1004+130. We have compared these to archival X-ray and UV data in order to investigate potential changes in the X-ray and UV absorption, and in the X-ray jet. We also combine both *Chandra* observations creating a deeper exposure with which to investigate the nature of the X-ray jet and diffuse X-ray emission in more detail than previously possible. We summarize our main results below.

1. The amount of intrinsic X-ray absorption present in PG 1004+130 does not appear to vary significantly between each of the 4 *Chandra* and *XMM-Newton* observations. In each case, the absorption can be well modeled with a partially covering absorber, or a partially ionized absorber (best-fitting spectral parameters are listed in Table 2). The low column densities, $N_{\text{H}} = 8 \times 10^{20} - 4 \times 10^{21} \text{ cm}^{-2}$ for a fully covering absorber, and lack of variability suggest that the absorption may not be due to the typical shielding gas invoked in quasar-wind models. See Sections 3.2 and 5.1.
2. The X-ray flux of PG 1004+130 varies by up to $\sim 40\%$ over 612 days (observed frame; see Figure 1), but re-

¹¹ <http://hea-www.harvard.edu/XJET/>

mains at least a factor of $15\times$ weaker than is expected for a typical RL quasar with a similar UV and radio luminosity. As the source does not show significant variability in the amount of X-ray absorption present, these changes are more likely related to intrinsic variations within the continuum source itself, or fluctuations in the jet. See Sections 3.1 and 5.1.

3. A strong C IV BAL is observed in our new 2014 *HST* COS observation, with $EW = 11.24 \pm 0.56 \text{ \AA}$. This is significantly variable, with an absolute change of $\Delta EW = 8.26 \pm 0.66 \text{ \AA}$ and a fractional change of $\Delta EW / \langle EW \rangle = 1.16 \pm 0.11$ from the previous 2003 *HST* STIS observation, 3183 days earlier in the rest-frame of PG 1004+130. While the absolute change in EW is not exceptional, the fractional change is one of the highest observed in a BAL quasar. See Sections 3.3 and 5.1.
4. An X-ray knot in the FRI radio jet is clearly detected in the combined, ~ 100 ks *Chandra* data (see Figure 5, top panels). It appears downstream from the peak of the radio emission, and at a distance of $\sim 8''$ (30 kpc) from the central X-ray source. It has a spatial extent of $\sim 4''$ (15 kpc). Its spatial and spectral properties are consistent with synchrotron emission from populations of shock-heated electrons. No similar X-ray counterpart to the FRII counterjet is detected. See Sections 4.1 and 5.2.
5. Asymmetric diffuse X-ray emission is detected around PG 1004+130, with a lower luminosity underlying the unseen counterjet to the NW ($L_{0.5-4\text{keV}} = 8.56_{-3.2}^{+4.5} \times 10^{41} \text{ erg s}^{-1}$) than the X-ray detected jet to the SE ($L_{0.5-4\text{keV}} = 1.81_{-0.44}^{+0.46} \times 10^{42} \text{ erg s}^{-1}$). In both cases a thermal model for the emission is disfavored and a non-thermal origin, possibly due to inverse Compton scattering of CMB photons, is more likely. The SE emission has a best-fitting power-law slope of $\Gamma = 1.65_{-0.74}^{+0.89}$, consistent with the value for the NW emission, $\Gamma = 1.95_{-1.05}^{+1.67}$. In both cases, the intensity of the emission decreases relatively smoothly, radially from the central source (see Figure 6, bottom). It extends out to $65''$ (250 kpc) to the SE and $55''$ (210 kpc) to the NW. See Sections 4.2 and 5.2.

In this work we have conducted a comprehensive, high S/N, multi-epoch, X-ray and UV spectral monitoring campaign of the RL BAL quasar PG 1004+130. The results determined here serve as a template for other RL BAL quasars. The logical next step would be to study systematically the properties of a larger sample of RL BALs (thus extending both this work and that of Miller et al. 2009, Saez et al. 2012, and Welling et al. 2014). However, the majority of such objects are not economical *Chandra* targets due to their high z and low X-ray fluxes. For example, to obtain 2 spectra with ~ 500 counts for each of the 12 snapshot targets from Miller et al. (2009) would require > 2 Ms of *Chandra* time. The forthcoming *Athena* observatory, with its larger effective area, will provide a better facility for this type of study.

AES, WNB, and BL gratefully acknowledge the support of *Chandra* X-ray Center grant G04-15093X, Space Telescope Science Institute grant HST-GO-13516.001-A, and NASA ADP grant NNX10AC99G. SCG thanks the Natural Science

and Engineering Research Council of Canada for support. The Guaranteed Time Observations (GTO) included here were selected by the ACIS Instrument Principal Investigator, Gordon P. Garmire, currently of the Huntingdon Institute for X-ray Astronomy, LLC, which is under contract to the Smithsonian Astrophysical Observatory; contract SV2-82024. This work was also based on observations obtained with *XMM-Newton*, an ESA science mission with instruments and contributions directly funded by ESA Member States and NASA. We thank Teddy Cheung for sharing radio data with us, and the anonymous referee for constructive comments.

Facilities: CXO (ACIS), XMM (EPIC), HST (COS).

REFERENCES

- Achterberg, A., Gallant, Y. A., Kirk, J. G., & Guthmann, A. W. 2001, *MNRAS*, 328, 393
- Arnaud, K. A. 1996, in *Astronomical Society of the Pacific Conference Series*, Vol. 101, *Astronomical Data Analysis Software and Systems V*, ed. G. H. Jacoby & J. Barnes, 17
- Bahcall, J. N., Kirhakos, S., Saxe, D. H., & Schneider, D. P. 1997, *ApJ*, 479, 642
- Bai, J. M., & Lee, M. G. 2003, *ApJ*, 585, L113
- Band, D. L., & Grindlay, J. E. 1986, *ApJ*, 308, 576
- Barlow, T. A. 1993, PhD thesis, California University
- Baskin, A., Laor, A., & Hamann, F. 2015, *ArXiv e-prints*, 1502.06609
- Becker, R. H., Gregg, M. D., Hook, I. M., et al. 1997, *ApJ*, 479, L93
- Becker, R. H., White, R. L., Gregg, M. D., et al. 2000, *ApJ*, 538, 72
- Becker, R. H., White, R. L., & Helfand, D. J. 1995, *ApJ*, 450, 559
- Blandford, R. D., & Koenigl, A. 1979, *Astrophys. Lett.*, 20, 15
- Brandt, W. N., Laor, A., & Wills, B. J. 2000, *ApJ*, 528, 637
- Brotherton, M. S., Laurent-Muehleisen, S. A., Becker, R. H., et al. 2005, *AJ*, 130, 2006
- Brotherton, M. S., van Breugel, W., Smith, R. J., et al. 1998, *ApJ*, 505, L7
- Bruni, G., González-Serrano, J. I., Pedani, M., et al. 2014, *A&A*, 569, A87
- Capellupo, D. M., Hamann, F., Shields, J. C., Halpern, J. P., & Barlow, T. A. 2013, *MNRAS*, 429, 1872
- Capellupo, D. M., Hamann, F., Shields, J. C., Rodríguez Hidalgo, P., & Barlow, T. A. 2011, *MNRAS*, 413, 908
- . 2012, *MNRAS*, 422, 3249
- Cash, W. 1979, *ApJ*, 228, 939
- Celotti, A., Ghisellini, G., & Chiaberge, M. 2001, *MNRAS*, 321, L1
- Croston, J. H., Hardcastle, M. J., Harris, D. E., et al. 2005, *ApJ*, 626, 733
- Dickey, J. M., & Lockman, F. J. 1990, *ARA&A*, 28, 215
- Drake, A. J., Djorgovski, S. G., Mahabal, A., et al. 2009, *ApJ*, 696, 870
- Elvis, M., & Fabbiano, G. 1984, *ApJ*, 280, 91
- Eracleous, M., & Halpern, J. P. 2004, *ApJS*, 150, 181
- Fan, L. L., Wang, H. Y., Wang, T., et al. 2009, *ApJ*, 690, 1006
- Fanaroff, B. L., & Riley, J. M. 1974, *MNRAS*, 167, 31P
- Filiz Ak, N., Brandt, W. N., Hall, P. B., et al. 2012, *ApJ*, 757, 114
- . 2013, *ApJ*, 777, 168
- Fomalont, E. B. 1981, in *IAU Symposium*, Vol. 94, *Origin of Cosmic Rays*, ed. G. Setti, G. Spada, & A. W. Wolfendale, 111–125
- Fruscione, A., McDowell, J. C., Allen, G. E., et al. 2006, in *Society of Photo-Optical Instrumentation Engineers (SPIE) Conference Series*, Vol. 6270, *Society of Photo-Optical Instrumentation Engineers (SPIE) Conference Series*
- Gallagher, S. C., Brandt, W. N., Chartas, G., & Garmire, G. P. 2002, *ApJ*, 567, 37
- Gallagher, S. C., Brandt, W. N., Chartas, G., et al. 2006, *ApJ*, 644, 709
- Gallagher, S. C., Brandt, W. N., Sambruna, R. M., Mathur, S., & Yamasaki, N. 1999, *ApJ*, 519, 549
- Gallagher, S. C., Brandt, W. N., Wills, B. J., et al. 2004, *ApJ*, 603, 425
- Garcia, A., Sodré, L., Jablonski, F. J., & Terlevich, R. J. 1999, *MNRAS*, 309, 803
- Garmire, G. P., Bautz, M. W., Ford, P. G., Nousek, J. A., & Ricker, Jr., G. R. 2003, in *Society of Photo-Optical Instrumentation Engineers (SPIE) Conference Series*, Vol. 4851, *X-Ray and Gamma-Ray Telescopes and Instruments for Astronomy*, ed. J. E. Truemper & H. D. Tananbaum, 28–44
- Gehrels, N. 1986, *ApJ*, 303, 336
- Ghisellini, G., Haardt, F., & Matt, G. 1994, *MNRAS*, 267, 743

- Gibson, R. R., Brandt, W. N., Gallagher, S. C., Hewett, P. C., & Schneider, D. P. 2010, *ApJ*, 713, 220
- Gibson, R. R., Brandt, W. N., Schneider, D. P., & Gallagher, S. C. 2008, *ApJ*, 675, 985
- Gibson, R. R., Jiang, L., Brandt, W. N., et al. 2009, *ApJ*, 692, 758
- Giustini, M., Cappi, M., & Vignali, C. 2008, *A&A*, 491, 425
- Giustini, M., Cappi, M., Chartas, G., et al. 2011, *A&A*, 536, A49
- Goodger, J. L., Hardcastle, M. J., Croston, J. H., et al. 2010, *ApJ*, 708, 675
- Gopal-Krishna, & Wiita, P. J. 2000, *A&A*, 363, 507
- Green, J. C., Froning, C. S., Osterman, S., et al. 2012, *ApJ*, 744, 60
- Green, P. J., & Mathur, S. 1996, *ApJ*, 462, 637
- Green, P. J., Scharrel, N., Anderson, S. F., et al. 1995, *ApJ*, 450, 51
- Gregg, M. D., Becker, R. H., & de Vries, W. 2006, *ApJ*, 641, 210
- Grier, C. J., Hall, P. B., Brandt, W. N., et al. 2015, *ArXiv e-prints*, 1503.03076
- Hardcastle, M. J., Worrall, D. M., Kraft, R. P., et al. 2003, *ApJ*, 593, 169
- Harris, D. E., Cheung, C. C., Biretta, J. A., et al. 2006, *ApJ*, 640, 211
- Harris, D. E., & Krawczynski, H. 2006, *ARA&A*, 44, 463
- Harrison, F. A., Craig, W. W., Christensen, F. E., et al. 2013, *ApJ*, 770, 103
- Hewett, P. C., & Foltz, C. B. 2003, *AJ*, 125, 1784
- Hinshaw, G., Larson, D., Komatsu, E., et al. 2013, *ApJS*, 208, 19
- Ishida, M., Tsujimoto, M., Kohmura, T., et al. 2011, *PASJ*, 63, 657
- Jansen, F., Lumb, D., Altieri, B., et al. 2001, *A&A*, 365, L1
- Jester, S., Harris, D. E., Marshall, H. L., & Meisenheimer, K. 2006, *ApJ*, 648, 900
- Kallman, T. R., & McCray, R. 1982, *ApJS*, 50, 263
- Kunert-Bajraszewska, M., Katarzyński, K., & Janiuk, A. 2015, *A&A*, 574, A110
- Laor, A., & Brandt, W. N. 2002, *ApJ*, 569, 641
- Lundgren, B. F., Wilhite, B. C., Brunner, R. J., et al. 2007, *ApJ*, 656, 73
- Luo, B., Brandt, W. N., Alexander, D. M., et al. 2013, *ApJ*, 772, 153
- , 2014, *ApJ*, 794, 70
- Lusso, E., Comastri, A., Vignali, C., et al. 2010, *A&A*, 512, A34
- Marshall, H. L., Carone, T. E., Peterson, B. M., et al. 1997, *ApJ*, 479, 222
- Marshall, H. L., Gelbord, J. M., Schwartz, D. A., et al. 2011, *ApJS*, 193, 15
- Mateos, S., Saxton, R. D., Read, A. M., & Sembay, S. 2009, *A&A*, 496, 879
- Matt, G., Brandt, W. N., & Fabian, A. C. 1996, *MNRAS*, 280, 823
- Menou, K., Vanden Berk, D. E., Ivezić, Ž., et al. 2001, *ApJ*, 561, 645
- Miller, B. P., Brandt, W. N., Gallagher, S. C., et al. 2006, *ApJ*, 652, 163, (M06)
- Miller, B. P., Brandt, W. N., Gibson, R. R., Garmire, G. P., & Shemmer, O. 2009, *ApJ*, 702, 911
- Miller, B. P., Brandt, W. N., Schneider, D. P., et al. 2011, *ApJ*, 726, 20
- Murray, N., Chiang, J., Grossman, S. A., & Voit, G. M. 1995, *ApJ*, 451, 498
- Nevalainen, J., David, L., & Guainazzi, M. 2010, *A&A*, 523, A22
- Page, K. L., Reeves, J. N., O'Brien, P. T., & Turner, M. J. L. 2005, *MNRAS*, 364, 195
- Proga, D., Stone, J. M., & Kallman, T. R. 2000, *ApJ*, 543, 686
- Reeves, J., Done, C., Pounds, K., et al. 2008, *MNRAS*, 385, L108
- Reeves, J. N., & Turner, M. J. L. 2000, *MNRAS*, 316, 234
- Rochais, T. B., DiPompeo, M. A., Myers, A. D., et al. 2014, *MNRAS*, 444, 2498
- Rogerson, J. A., Hall, P. B., Snedden, S. A., Brotherton, M. S., & Anderson, S. F. 2011, *New Astron.*, 16, 128
- Runnoe, J. C., Ganguly, R., Brotherton, M. S., & DiPompeo, M. A. 2013, *MNRAS*, 433, 1778
- Rupke, D. S., Veilleux, S., & Sanders, D. B. 2002, *ApJ*, 570, 588
- Saez, C., Brandt, W. N., Gallagher, S. C., Bauer, F. E., & Garmire, G. P. 2012, *ApJ*, 759, 42
- Saez, C., Brandt, W. N., Shemmer, O., et al. 2011, *ApJ*, 738, 53
- Sambruna, R. M., Eracleous, M., & Mushotzky, R. F. 1999, *ApJ*, 526, 60
- Sambruna, R. M., Gambill, J. K., Maraschi, L., et al. 2004, *ApJ*, 608, 698
- Schlaflly, E. F., & Finkbeiner, D. P. 2011, *ApJ*, 737, 103
- Schwartz, D. A., Marshall, H. L., Lovell, J. E. J., et al. 2006, *ApJ*, 647, L107
- Scott, A. E., Stewart, G. C., & Mateos, S. 2012, *MNRAS*, 423, 2633
- Scott, A. E., Stewart, G. C., Mateos, S., et al. 2011, *MNRAS*, 417, 992
- Shankar, F., Dai, X., & Sivakoff, G. R. 2008, *ApJ*, 687, 859
- Shen, Y., Richards, G. T., Strauss, M. A., et al. 2011, *ApJS*, 194, 45
- Sim, S. A., Proga, D., Kurosawa, R., et al. 2012, *MNRAS*, 426, 2859
- Sim, S. A., Proga, D., Miller, L., Long, K. S., & Turner, T. J. 2010, *MNRAS*, 408, 1396
- Smith, A. G., Nair, A. D., Leacock, R. J., & Clements, S. D. 1993, *AJ*, 105, 437
- Stalin, C. S., Gopal-Krishna, Sagar, R., & Wiita, P. J. 2004, *MNRAS*, 350, 175
- Steffen, A. T., Strateva, I., Brandt, W. N., et al. 2006, *AJ*, 131, 2826
- Stocke, J. T., Morris, S. L., Weymann, R. J., & Foltz, C. B. 1992, *ApJ*, 396, 487
- Strateva, I. V., Brandt, W. N., Schneider, D. P., Vanden Berk, D. G., & Vignali, C. 2005, *AJ*, 130, 387
- Streblyanska, A., Barcons, X., Carrera, F. J., & Gil-Merino, R. 2010, *A&A*, 515, A2
- Strüder, L., Briel, U., Dennerl, K., et al. 2001, *A&A*, 365, L18
- Tananbaum, H., Avni, Y., Branduardi, G., et al. 1979, *ApJ*, 234, L9
- Tavecchio, F., Maraschi, L., Sambruna, R. M., & Urry, C. M. 2000, *ApJ*, 544, L23
- Teng, S. H., Brandt, W. N., Harrison, F. A., et al. 2014, *ApJ*, 785, 19
- Tsujimoto, M., Guainazzi, M., Plucinsky, P. P., et al. 2011, *A&A*, 525, A25
- Turner, M. J. L., Abbey, A., Arnaud, M., et al. 2001, *A&A*, 365, L27
- Verner, D. A., & Ferland, G. J. 1996, *ApJS*, 103, 467
- Véron-Cetty, M.-P., & Véron, P. 2010, *A&A*, 518, A10
- Vestergaard, M., & Peterson, B. M. 2006, *ApJ*, 641, 689
- Vignali, C., Brandt, W. N., & Schneider, D. P. 2003, *AJ*, 125, 433
- Vilkoviskij, E. Y., & Irwin, M. J. 2001, *MNRAS*, 321, 4
- Voges, W., Aschenbach, B., Boller, T., et al. 1999, *A&A*, 349, 389
- Weisskopf, M. C., Tananbaum, H. D., Van Speybroeck, L. P., & O'Dell, S. L. 2000, in *Society of Photo-Optical Instrumentation Engineers (SPIE) Conference Series*, Vol. 4012, *X-Ray Optics, Instruments, and Missions III*, ed. J. E. Truemper & B. Aschenbach, 2–16
- Welling, C. A., Miller, B. P., Brandt, W. N., Capellupo, D. M., & Gibson, R. R. 2014, *MNRAS*, 440, 2474
- Weymann, R. J., Morris, S. L., Foltz, C. B., & Hewett, P. C. 1991, *ApJ*, 373, 23
- Wildy, C., Goad, M. R., & Allen, J. T. 2014, *MNRAS*, 437, 1976
- Willingale, R., Starling, R. L. C., Beardmore, A. P., Tanvir, N. R., & O'Brien, P. T. 2013, *MNRAS*, 431, 394
- Wills, B. J., Brandt, W. N., & Laor, A. 1999, *ApJ*, 520, L91
- Wilms, J., Allen, A., & McCray, R. 2000, *ApJ*, 542, 914
- Woodgate, B. E., Kimble, R. A., Bowers, C. W., et al. 1998, *PASP*, 110, 1183
- Worrall, D. M. 2009, *A&A Rev.*, 17, 1
- Worrall, D. M., Tananbaum, H., Giommi, P., & Zamorani, G. 1987, *ApJ*, 313, 596
- Wu, J., Brandt, W. N., Comins, M. L., et al. 2010, *ApJ*, 724, 762
- York, D. G., Adelman, J., Anderson, Jr., J. E., et al. 2000, *AJ*, 120, 1579
- Young, M., Elvis, M., & Risaliti, G. 2010, *ApJ*, 708, 1388
- Zamorani, G., Henry, J. P., Maccacaro, T., et al. 1981, *ApJ*, 245, 357